Multi-particle collision dynamics with a non-ideal equation of state. I

Arne W. Zantop, and Holger Stark

View Online   Export Citation   CrossMark

ARTICLES YOU MAY BE INTERESTED IN

Multi-particle collision dynamics with a non-ideal equation of state. I

View Online   Export Citation   CrossMark

Arne W. Zantop [ID] and Holger Stark[a] [ID]

AFFILIATIONS

Institute of Theoretical Physics, Technische Universität Berlin, Hardenbergstraße 36, 10623 Berlin, Germany

[a]Author to whom correspondence should be addressed: holger.stark@tu-berlin.de

ABSTRACT

The method of multi-particle collision dynamics (MPCD) and its different implementations are commonly used in the field of soft matter physics to simulate fluid flow at the micron scale. Typically, the coarse-grained fluid particles are described by the equation of state of an ideal gas, and the fluid is rather compressible. This is in contrast to conventional fluids, which are incompressible for velocities much below the speed of sound, and can cause inhomogeneities in density. We propose an algorithm for MPCD with a modified collision rule that results in a non-ideal equation of state and a significantly decreased compressibility. It allows simulations at less computational costs compared to conventional MPCD algorithms. We derive analytic expressions for the equation of state and the corresponding compressibility as well as shear viscosity. They show overall very good agreement with simulations, where we determine the pressure by simulating a quiet bulk fluid and the shear viscosity by simulating a linear shear flow and a Poiseuille flow.

I. INTRODUCTION

Since their introduction in 1999,[1] algorithms belonging to the method of multi-particle collision dynamics (MPCD) have become a standard tool to simulate fluid flows in the field of soft matter physics.[2–4] In particular, MPCD algorithms have commonly been used to model solvent dynamics in the context of microswimmers,[5–18] where we can only cite a few examples. Further studies address colloidal suspensions,[19–23] polymers,[24–26] blood cells,[27] the African trypanosome as the causative agent of the sleeping sickness,[28] and even fish schools.[29] Also, extensions to binary and ternary fluid mixtures,[30–32] liquid crystals,[33–35] and chemically reacting systems[36] exist. MPCD methods are particularly suited to simulate solvent flow on the microscopic scale because they solve the Navier–Stokes equations but also incorporate the omnipresent thermal fluctuations.[1,37] The particle-based strategy of MPCD makes the implementation of no-slip boundary conditions in complex geometries very straightforward.[38] Furthermore, the collision rules for the coarse-grained fluid particles are well suited for the implementation on parallel computer hardware[39,40] so that extensive simulations can also be performed on desktop computers with graphic cards.

Although MPCD methods are often used to simulate the dynamics of incompressible solvents, one has to be aware that the coarse-grained fluid particles follow the equation of state of an ideal gas.[1,32,41] Therefore, the fluid is rather compressible and has a low speed of sound c_s.[21] This is tolerable for typical flow velocities well below c_s. In contrast, in the presence of large pressure gradients, pronounced inhomogeneities in the fluid density can occur due to the high compressibility. For example, such a situation has recently been observed in strongly clustered microswimmers,[12] where the overlapping flow fields of many microswimmers are responsible for strong pressure gradients. While variations in fluid density are, in principal, necessary to generate pressure gradients, these variations need to be small to stay close to the limit of an incompressible fluid. Thus, the compressibility needs to be sufficiently small. For the MPCD fluid with its ideal-gas equation of state, this can be achieved by increasing the number n_0 of fluid particles per collision cell and thereby density.[12] However, such an approach causes an immense increase in the simulation time proportional to the square of the fluid density n_0^2 if the system size should be kept constant at an equal Péclet number.

In this paper, we follow a different strategy to decrease compressibility. All the MPCD algorithms consist of a sequence of collision and streaming steps. Here, we propose a new collision rule that results in a non-ideal equation of state for the MPCD fluid. Note that such non-ideal equations of state are required and have

already been introduced in the context of simulating fluid mixtures within MPCD.[31,32] Thus, compressibility is reduced for the constant particle number n_0, and the computational efficiency is enhanced compared to conventional MPCD algorithms, which need to employ a larger particle density. Our approach extends ideas of Tüzel, Ihle, and collaborators, who included geometric properties of hard-core particles in two dimensions into the collision rule to control momentum transport in the fluid.[42,43] This approach has also been extended to the simulation of fluid mixtures.[30] In contrast to conventional MPCD algorithms, where collisions take place at a fixed rate $1/\Delta t$, collisions instead occur stochastically with a probability that depends on the local density and velocities. In the present work, we extent the approach of Refs. 42 and 43 to three dimensions and strongly modify the geometric rules of the collision so that they can be implemented in an existing MPCD code more easily. Furthermore, our new collision rule allows us to keep the typical canonical thermostat and also to take care of angular momentum conservation during collisions, which is particularly important for the simulation of colloids and active particles.[44]

This article is structured as follows: In Sec. II, we introduce the extended MPCD method with its new collision rule including three possible collision probabilities. Then, we derive approximate analytic expressions for the equation of state and the associated compressibility in Sec. III as well as the shear viscosity in Sec. IV. For the shear viscosity, we consider both contributions that arise from the streaming and collision step of the extended MPCD method. In Sec. V, we compare these analytic expressions with the results from simulations and obtain very good agreement for the equation of state. In particular, we demonstrate the reduction of the compressibility for reasonable particle densities. We measure the shear viscosity by determining the collisional and streaming viscosities in a linear shear flow geometry. The total viscosity agrees very well with values determined from simulating a Poiseuille flow and also with the analytic expression above a density of $\sim n_0 = 20$. We close with conclusions and an outlook in Sec. VI.

II. ALGORITHM OF THE EXTENDED MPCD METHOD

Our method shares the common features typical for the group of MPCD algorithms.[1,3,45] Like all MPCD algorithms, it considers point-like particles that represent the fluid at a mesoscopic level of description. They perform a sequence of streaming and collision steps. Since the latter conserves linear momentum, the resulting hydrodynamic flow fields fulfill the Navier–Stokes equations.[1] While we perform the steaming step as in other MPCD algorithms, we alter the collision step as already mentioned in the Introduction. We now explain the extended MPCD method in more detail.

During the streaming step (i), the point particles with masses m_0, positions $\mathbf{x}_i(t)$, and velocities $\mathbf{v}_i(t)$ move ballistically during time Δt,

$$\mathbf{x}_i(t + \Delta t) = \mathbf{x}_i(t) + \mathbf{v}_i(t)\Delta t. \tag{1}$$

They collide with confining walls or moving objects such as model microswimmers called squirmers[4,8,9,16–18] and thereby transfer both linear and angular momentum to these moving objects. By applying the so-called bounce-back rule,[1,38] the collisions either enforce the no-slip boundary condition at confining walls and passive colloids or the slip-velocity field, which are present at squirmer surfaces.

For the collision step (ii), we suggest an alternative algorithm compared to the original SRD method[1] or the collision operator based on the Andersen thermostat.[4] As in all MPCD algorithms, the simulation volume is divided by a cubic lattice and the fluid particles are grouped into the cubic unit cells of linear size a_0 centered around $\boldsymbol{\xi}$ and with volume $\mathcal{V}_{\boldsymbol{\xi}}$. Each cell then contains $n_{\boldsymbol{\xi}}$ particles with the mean velocity $\mathbf{v}_{\boldsymbol{\xi}}$ and center-of-mass position $\mathbf{x}_{\boldsymbol{\xi}}$. Additionally, each cell is divided into two halves A and B by a plane $P_{\mathbf{x}_{\boldsymbol{\xi}},\hat{\mathbf{n}}}$ through the center-of-mass position $\mathbf{x}_{\boldsymbol{\xi}}$[46] and with an orientation defined by the unit normal vector $\hat{\mathbf{n}}$ [see Fig. 1(a)]. For each cell, $\hat{\mathbf{n}}$ is randomly drawn from a discrete set of 13 possible orientations at each collision step. By definition, $\hat{\mathbf{n}}$ always points to region A. The number of particles on each side of the plane is denoted by n_A and n_B, respectively. Their mean velocities $\bar{v}_A$ and $\bar{v}_B$, respectively, along the normal vector $\hat{\mathbf{n}}$ are given relative to $\mathbf{v}_{\boldsymbol{\xi}}$.

The main idea of the new collision step is that the particles in region A and B only collide when they move toward each other. Then, they stochastically exchange a momentum $m_0\delta v_i$ along $\hat{\mathbf{n}}$ both with particles in the same half A, B and also on the other side of the plane. The latter mechanism generates momentum flux across the randomly oriented plane and thereby contributes to pressure, which belongs to the isotropic part of the stress tensor.

The collision step can be summarized by

$$\mathbf{v}_i^{\text{new}} = \mathbf{v}_i + \chi(\Delta u)\{\hat{\mathbf{n}}\,[\,\hat{\mathbf{n}} \cdot (\mathbf{v}_{\boldsymbol{\xi}} - \mathbf{v}_i) + \delta\mathbf{v}_i\,]$$
$$- \mathbf{I}_{\boldsymbol{\xi}}^{-1} m_0 \sum_{\mathbf{x}_j \in \mathcal{V}_{\boldsymbol{\xi}}} [\,\mathbf{x}_{j,c} \times \hat{\mathbf{n}}\,(\delta v_j - \hat{\mathbf{n}} \cdot \mathbf{v}_j)\,] \times \mathbf{x}_{i,c}\}, \tag{2}$$

where $\mathbf{x}_{i,c}$ denotes the position vector of particle i relative to the center-of-mass position $\mathbf{x}_{\boldsymbol{\xi}}$. As we explain below, the collision between the particles in region A and B occurs with a certain probability. To initiate a collision, the stochastic variable $\chi(\Delta u)$ is set to one; otherwise, it is zero. The term following $\chi(\Delta u)$ in the square brackets sets the normal velocity components of all particles i to the normal component of the center-of-mass velocity, $\hat{\mathbf{n}} \cdot \mathbf{v}_{\boldsymbol{\xi}}$. Then, new values for the relative velocity component δv_i are assigned as explained below. They all add up to zero in order to preserve the total momentum. The second term in the curly brackets is added to conserve the angular momentum. Thus, the value $L_{\boldsymbol{\xi}} = m_0 \sum_{\mathbf{x}_i \in \mathcal{V}_{\boldsymbol{\xi}}} \mathbf{x}_i \times \mathbf{v}_i$

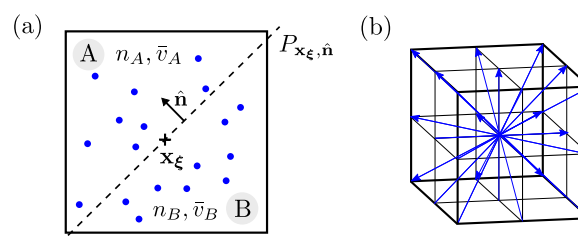**FIG. 1**. (a) Side view of a collision cell with the dividing plane $P_{\mathbf{x}_{\boldsymbol{\xi}},\hat{\mathbf{n}}}$ through the center-of-mass position $\mathbf{x}_{\boldsymbol{\xi}}$ and unit normal vector $\hat{\mathbf{n}}$. (b) 13 possible collision or normal vectors $\hat{\mathbf{n}}$ that point to the corners as well as centers of surfaces and edges of the collision cell.

before the collision is preserved. Here, $\mathbf{I}_\xi$ is the moment-of-inertia tensor of all particles in the cell relative to the center of mass.

We have already introduced the mean values of the normal velocity components $\bar{v}_A$ and $\bar{v}_B$ on either side of the collision plane. Then, collisions between the particles of region A and B occur, when, on average, they move toward each other, meaning that the relative velocity

$$\Delta u = \bar{v}_B - \bar{v}_A \tag{3}$$

is positive. Furthermore, collisions between the particle clouds in A and B occur with the rate $c \Delta u n_A n_B$, where c quantifies the scattering cross section. A similar term has been used for the collision rate of two clouds of hard-core particles or in chemical reactions of the second order[47] and can be motivated by the collision term in the Boltzmann equation.[48] Thus, the probability that a collision occurs or that the stochastic variable $\chi(\Delta u)$ is set to one becomes

$$p_\chi(\Delta u) \equiv \Theta(\Delta u)\, c\, \Delta u\, n_A\, n_B \tag{4}$$

$$\approx \Theta(\Delta u)\big[1 - \exp(-c\,\Delta u\, n_A\, n_B)\big]. \tag{5}$$

Here, $\Theta(\Delta u)$ is the Heaviside step function so that collisions only occur for $\Delta u > 0$. In the second line, assuming a sufficiently small c, we have introduced the exponential that guarantees $p_\chi(\Delta u) \le 1$. Another possibility to fulfill this constraint using Eq. (4) is[30]

$$p_\chi(\Delta u) = \begin{cases} \Theta(\Delta u)\, c\, \Delta u\, n_A\, n_B & \text{for } p_\chi(\Delta u) \le 1 \\ 1 & \text{else.} \end{cases} \tag{6}$$

We will explore also this form in Sec. V B when we calculate the pressure in the MPCD simulations.

Finally, we introduce the changes δv_i in the velocity component along the normal $\hat{\mathbf{n}}$. It consists of two contributions: $\delta v_i = \delta v_i^t + \delta v_i^s$. The first term transfers momentum from region B of the cell to particles i in the region A and vice versa,

$$\delta v_i^t \equiv \frac{n_{B/A}}{n_{A/B}}\, \bar{v}_{B/A}. \tag{7}$$

Here, the first indices apply to particles i in region A that take over the momentum $m_0 \bar{v}_B$ from region B and the second indices apply to particles i in region B. The ratios n_B/n_A and n_A/n_B guarantee the overall momentum conservation, meaning the total momenta from regions A and B are just swapped. The second contribution,

$$\delta v_i^s \equiv \delta v_i^{\mathrm{MB}} - \Delta v_{A/B}, \tag{8}$$

assigns each particle a random velocity δv_i^{MB} drawn from a Maxwell–Boltzmann distribution at temperature T, which serves as a thermostat for the fluid. We subtract the mean random velocity

$$\Delta v_{A/B} = \frac{1}{n_{A/B}} \sum_{\{\mathbf{x}_i \in \mathscr{V}_{A/B}\}} \delta v_i^{\mathrm{MB}} \tag{9}$$

to preserve total momentum in both regions A and B, separately.

In particular, the introduction of the momentum transfer in Eq. (7) and the transfer rate Eq. (5) defines the equation of state. As shown in Sec. III, it contains a term proportional to n_ξ^2 resembling a virial expansion and thus extends the ideal gas term.

As in other MPCD algorithms, immersed boundaries are represented by the so-called "ghost" particles during the collision step.[38] These are added to the collision cells to interact with the other fluid particles. In simulations with squirmers, the ghost particles are assigned the local velocity of the translating and rotating squirmers plus a random thermal velocity drawn from a Boltzmann distribution. Then, the changes in linear and angular momentum of the ghost particles following from step (ii) are assigned to the relevant squirmer, which ensures that linear and angular momentum are conserved. Finally, before performing each collision step, the lattice is randomly shifted to ensure Galilean invariance.[49]

III. EQUATION OF STATE

To calculate the equation of state, we use the definition of pressure as the normal component of the momentum flux through an arbitrarily oriented plane.[50] In the extended MPCD method, both streaming (i) and collision step (ii) contribute to the pressure,

$$P = P_{\mathrm{coll}} + P_{\mathrm{str}}. \tag{10}$$

During the streaming step (i), particles do not interact and simply transport momentum across a plane. This results in the ideal gas contribution $P_{\mathrm{str}} = n k_B T / a_0^3$, which we already know from the conventional MPCD methods.[32]

To evaluate the contribution P_{coll} from the collision step (ii), we consider the momentum flux across a plane with area a_0^2 that lies in a single collision cell. Without loss of generality, we choose the plane $P_{\hat{\mathbf{y}}, y_0}$ perpendicular to the $\hat{\mathbf{y}}$ axis at position y_0 and then average over all y_0 (see Fig. 2). During the collision step, momentum is transported from the region $y < y_0$ across the plane $P_{\hat{\mathbf{y}}, y_0}$ into $y > y_0$ during time Δt. Thus, for the pressure as momentum transfer per area and time, we obtain

$$P_{\mathrm{coll}} = \frac{m_0}{a_0^2 \Delta t} \left\langle \hat{\mathbf{y}} \cdot \sum_{\{i \,|\, y_i > y_0\}} \left(\mathbf{v}_i^{\mathrm{new}} - \mathbf{v}_i\right) \right\rangle. \tag{11}$$

Here, i is restricted to all particles above $P_{\hat{\mathbf{y}}, y_0}$ and $m_0 \hat{\mathbf{y}} \cdot (\mathbf{v}_i^{\mathrm{new}} - \mathbf{v}_i)$ is the change in the normal momentum component of particle i during
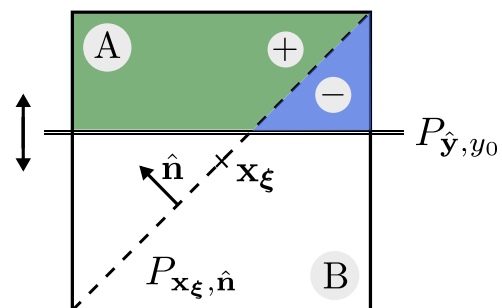
FIG. 2. To derive the equation of state, we consider the momentum transferred to the region above the plane $P_{\hat{\mathbf{y}}, y_0}$ with unit normal vector $\hat{\mathbf{y}}$ and at position $y = y_0$. Note that to evaluate $\mathrm{sign}(\mathbf{x} \cdot \hat{\mathbf{n}})$ in Eq. (15), one has to distinguish particles that are located in the green region as part of region A relative to the collision plane with normal $\hat{\mathbf{n}}$ and particles in the blue region as part of B.

collision and given in Eq. (2). The average goes over all possible collisions, particle configurations, orientations $\hat{\mathbf{n}}$ of the collision planes, and positions y_0. The term added to Eq. (2) in the second line to preserve angular momentum does not contribute to P_{coll} since it vanishes when averaging over all possible collisions. Furthermore, since particle i is either in region A and B and we average over all particle velocities relative to $\mathbf{v}_\xi$ with identical velocity distributions, we can ultimately replace $\hat{\mathbf{n}} \cdot (\mathbf{v}_\xi - \mathbf{v}_i)$ in Eq. (2) by the mean velocities $-\bar{v}_{A/B}$ in region A or B of the collision cell. Note that $\bar{v}_{A/B}$ are given relative to $\hat{\mathbf{n}} \cdot \mathbf{v}_\xi$. The choice of index A or B depends on the location of particle i. Thus, we can simplify Eq. (11) to

$$P_{\text{coll}} = \frac{m_0}{a_0^2 \Delta t} \left\langle \chi(\Delta u) \, \hat{\mathbf{y}} \cdot \hat{\mathbf{n}} \sum_{\{i|y_i > y_0\}} \delta v_i - \bar{v}_{A/B} \right\rangle. \quad (12)$$

The stochastic contribution δv_i^s of δv_i given in Eq. (8) obeys a Gaussian distribution with zero mean and therefore vanishes on average. The remaining part δv_i^t given in Eq. (7) becomes $\bar{v}_{B/A}$ using $n_{A/B} \approx n_\xi/2$. Thus, with the definition of the collision velocity Δu in Eq. (3), we can finally replace $\delta v_i - \bar{v}_{A/B}$ by $\bar{v}_{B/A} - \bar{v}_{A/B} = \Delta u \, \text{sign}(\mathbf{x}_i \cdot \hat{\mathbf{n}})$. The factor $\text{sign}(\mathbf{x}_i \cdot \hat{\mathbf{n}})$ comes in since the first index in $\bar{v}_{B/A} - \bar{v}_{A/B}$ applies if particle i is in region A, while the second index refers to a particle i in B (see Fig. 2). Noting also that Δu and $\mathbf{x}_i$ are independent stochastic variables, we can factorize the average in Eq. (12) and rewrite it as

$$P_{\text{coll}} = \frac{m_0}{a_0^2 \Delta t} \langle \chi(\Delta u) \Delta u \rangle \left\langle \hat{\mathbf{y}} \cdot \hat{\mathbf{n}} \sum_{\{i|y_i > y_0\}} \text{sign}(\mathbf{x}_i \cdot \hat{\mathbf{n}}) \right\rangle, \quad (13)$$

where

$$\langle \chi(\Delta u) \Delta u \rangle = \int_0^\infty \Delta u \, p_\chi(\Delta u) \, p(\Delta u) \, d\Delta u. \quad (14)$$

Here, $p(\Delta u)$ is the probability distribution for Δu and $p_\chi(\Delta u)$ is the probability for a collision to take place, as introduced in Sec. II.

We now calculate the two averages of Eq. (13). In the second average, we replace the conditional sum by a volume integral introducing the factor $n_\xi/a_0^3 \, \Theta(y - y_0)$ and average over y_0. We write the second average as $n_\xi \alpha_P$, where we identify the purely geometrical factor

$$\alpha_P \equiv \left\langle \frac{\hat{\mathbf{y}} \cdot \hat{\mathbf{n}}}{a_0^4} \int_{\mathscr{V}_\xi} \int_{-a_0/2}^{a_0/2} \text{sign}(\mathbf{x} \cdot \hat{\mathbf{n}}) \Theta(y - y_0) \, dy_0 dV \right\rangle_{\hat{\mathbf{n}}}. \quad (15)$$

It is the difference between the green and blue volume in Fig. 2 averaged over all $\hat{\mathbf{n}}$ and y_0 and weighted by the projection of $\hat{\mathbf{n}}$ on $\hat{\mathbf{y}}$. The integrals can be calculated for each of the 13 normal vectors $\hat{\mathbf{n}}$ so that we obtain in total

$$\alpha_P = \frac{1}{26} \left[\frac{1}{2} + 4 \left(\frac{1}{3\sqrt{2}} + \frac{13}{48\sqrt{3}} \right) \right] \approx 0.08. \quad (16)$$

For the second average, we need the probability distribution for $\Delta u = \bar{v}_B - \bar{v}_A$. Since the components of the single-particle velocities are Gaussian distributed with variance $k_B T/m_0$, also Δu is Gaussian distributed with variance $4 k_B T/(m_0 n_\xi)$, as shown in Appendix A using $n_A = n_B \approx n_\xi/2$. Taking the collision probability from Eq. (4),

we then have

$$\langle \chi(\Delta u) \Delta u \rangle = c \, n_A \, n_B \langle \Theta(\Delta u) \, \Delta u^2 \rangle = c \, n_\xi \frac{k_B T}{2 m_0}. \quad (17)$$

Thus, in total, we obtain from Eq. (13) for the pressure contribution of the collision step,

$$P_{\text{coll}} = \frac{c \alpha_P}{2 a_0^2 \Delta t} k_B T n_\xi^2, \quad (18)$$

which is quadratic in the particle density n_ξ. Hence, up to second order in density, the full equation of state reads

$$P a_0^3 = (P_{\text{str}} + P_{\text{coll}}) a_0^3 = n_\xi k_B T \left(1 + \frac{c a_0 \alpha_P}{2 \Delta t} n_\xi \right). \quad (19)$$

This gives a compressibility

$$\beta = \frac{1}{n_\xi} \frac{\partial n_\xi}{\partial P} = \frac{a_0^3}{n_\xi k_B T} \frac{1}{1 + c \alpha_P a_0 n_\xi / \Delta t}, \quad (20)$$

where the ideal gas contribution from the streaming step, $\beta_{\text{id}} = a_0^3/(n_\xi k_B T)$, is diminished by the second-order contribution from the collision step. This means that the MPCD fluid is less compressible.

We add two comments. First, if we take for the collision probability $p_\chi(\Delta u)$ the expression from Eq. (5), which we use as one option in the simulations, one can still evaluate $\langle \chi(\Delta u) \Delta u \rangle$ and then obtain the pressure contribution from the collision step,

$$P_{\text{coll}} = \frac{\alpha_P c \, k_B T n_\xi^2}{2 a_0^2 \Delta t} \exp\left(\frac{c^2 k_B T}{8 m_0} n_\xi^3 \right) \text{erfc}\left(\sqrt{\frac{k_B T}{2 m_0}} \frac{c n_\xi^3}{2} \right)$$

$$= \frac{c \alpha_P}{2 a_0^2 \Delta t} k_B T n_\xi^2 \left[1 - c \sqrt{\frac{k_B T n_\xi^3}{2\pi}} \right] + \mathcal{O}(n_\xi^5). \quad (21)$$

We will use this form when comparing the pressure in the simulations to the analytic result. Second, in deriving P_c, we have always set $n_A = n_B \approx n_\xi/2$, thus neglecting fluctuations in the particle numbers in regions A and B. For sufficiently large particle numbers, these fluctuations are small. When we compare our analytic results to simulations, we obtain good agreement and the approximation seems to be reasonable.

IV. SHEAR VISCOSITY

To derive an expression for the dynamic shear viscosity η, we consider the linear shear flow

$$\mathbf{v}(y) = \dot{\gamma} y \hat{\mathbf{x}} \quad (22)$$

with constant shear rate $\dot{\gamma}$ (see Fig. 3). We also note that the non-vanishing component of the viscous stress tensor, $\sigma_{xy} = \eta \partial_y v_x = \eta \dot{\gamma}$, describes the negative flux of the x component of momentum along the y direction. Similar to the derivation of the equation of state in Sec. III, the viscosity consists of two contributions from the collision and streaming step, respectively,

$$\eta = \eta_{\text{coll}} + \eta_{\text{str}}. \quad (23)$$

While the derivation of the collisional viscosity η_{coll} requires similar steps used in calculating the collisional contribution of pressure,

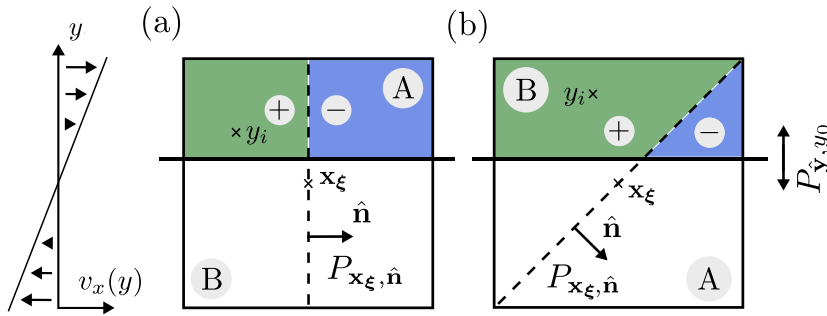**FIG. 3**. To derive the shear viscosity, we apply the shear flow $\mathbf{v}(y) = \dot{\gamma} y \hat{\mathbf{x}}$ and consider the momentum transferred to the region above the plane $P_{\hat{\mathbf{y}}, y_0}$ with unit normal vector $\hat{\mathbf{y}}$ and at position $y = y_0$. Examples for collision planes with $y_A = 0$ (a) and $y_A \neq 0$ (b) are shown.

the streaming viscosity η_{str} needs special attention. We start with the derivation of η_{coll}.

A. Collisional viscosity

Similar to our derivation of the pressure starting from Eq. (11), we consider the momentum transported during the collision step from the region $y < y_0$ across the plane $P_{\hat{\mathbf{y}}, y_0}$ into $y > y_0$ during time Δt (see Fig. 3). However, for σ_{xy}, we need the transfer of the x component of momentum per area and time, and thus,

$$\sigma_{xy} = -\frac{m_0}{a_0^2 \Delta t} \left\langle \hat{\mathbf{x}} \cdot \sum_{i|y_i > y_0} \mathbf{v}_i^{\text{new}} - \mathbf{v}_i \right\rangle. \quad (24)$$

When evaluating the term in the angular bracket using Eq. (2), we concentrate on the first line of Eq. (2) and then at the end following Ref. 45 to include angular momentum conservation, which is the origin of the second line. Replacing δv_i in Eq. (2) by $\bar{v}_{B/A}$ as before in Sec. III, we obtain

$$\sigma_{xy} = -\frac{m_0}{a_0^2 \Delta t} \left\langle \chi(\Delta u) \, \hat{\mathbf{x}} \cdot \hat{\mathbf{n}} \sum_{i|y_i > y_0} [\bar{v}_{B/A} + \hat{\mathbf{n}} \cdot (\mathbf{v}_\xi - \mathbf{v}_i)] \right\rangle.$$

On average, the relative velocity $\Delta u = \bar{v}_B - \bar{v}_A$ is equally distributed on the mean velocities of regions A and B so that we can use $\Delta u/2 \approx \bar{v}_A = -\bar{v}_B$. Furthermore, on average, $\mathbf{v}_\xi$ can be replaced by $\mathbf{v}_i/n_\xi$,[51] and we arrive at

$$\sigma_{xy} = -\frac{m_0}{a_0^2 \Delta t} \left\langle \chi(\Delta u) \, \hat{\mathbf{x}} \cdot \hat{\mathbf{n}} \sum_{i|y_i > y_0} \text{sign}(\mathbf{x}_i \cdot \hat{\mathbf{n}}) \frac{\Delta u}{2} - \hat{\mathbf{n}} \cdot \mathbf{v}_i \left(1 - \frac{1}{n_\xi}\right) \right\rangle. \quad (25)$$

As explained in Sec. III, $\text{sign}(\mathbf{x}_i \cdot \hat{\mathbf{n}})$ is necessary to distinguish between particle i being in either region A or B.

Now, we need to introduce the shear rate $\dot{\gamma}$ from the applied linear shear profile of Eq. (22). It comes in by setting $\mathbf{v}_i$ equal to its deterministic part $\dot{\gamma} y_i \hat{\mathbf{x}}$ and through the Gaussian distribution of Δu. In Appendix B, we show that the conditional distribution for Δu, given the collision vector $\hat{\mathbf{n}}$ and fixed position $\mathbf{x}_i$ of particle i, is Gaussian with the mean value

$$\mu_{i,\hat{\mathbf{n}}} = \langle \Delta u \rangle_{i,\hat{\mathbf{n}}} = -2 \dot{\gamma} \, \hat{\mathbf{x}} \cdot \hat{\mathbf{n}} \, \frac{y_A (n_\xi - 1) + \text{sign}(\mathbf{x}_i \cdot \hat{\mathbf{n}}) y_i}{n_\xi}. \quad (26)$$

The first factor originates from the orientation of the collision plane with collision vector $\hat{\mathbf{n}}$ relative to the shearing direction $\hat{\mathbf{x}}$ and the second factor from keeping particle i at fixed height y_i. The quantity y_A is the y coordinate of the center of mass of region A defined by the collision plane. For the different collision vectors $\hat{\mathbf{n}}$, we give them in Table I. We need this conditional mean value $\mu_{i,\hat{\mathbf{n}}} = \langle \Delta u \rangle_{i,\hat{\mathbf{n}}}$ when averaging over Δu since in Eq. (25), we also average over the position of particle i. Now, to evaluate the shear viscosity, it is sufficient to only consider the terms of σ_{xy} linear in the shear rate $\dot{\gamma}$. As we demonstrate in the following, they result from either thermal fluctuations of Δu or the deterministic part of $\mathbf{v}_i$ equal to $\dot{\gamma} y_i \hat{\mathbf{x}}$. Thermal fluctuations of $\mathbf{v}_i$ can be neglected since they produce higher-order terms in $\dot{\gamma}$.

To perform the average over Δu in Eq. (25), we first evaluate the required averages using the conditional distribution $p(\Delta u - \mu_{i,\hat{\mathbf{n}}})$ (see Appendix C). Since the shear-induced shift $\mu_{i,\hat{\mathbf{n}}}$ is small compared to the width of the distribution, $m_0 \mu_{i,\hat{\mathbf{n}}}^2 / k_B T \ll 1$, we can always linearize in $\mu_{i,\hat{\mathbf{n}}} \propto \dot{\gamma}$. First, for the mean conditional collision rate using Eq. (4) for $p_\chi(\Delta u)$, we obtain

$$\langle \chi(\Delta u) \rangle = \int_0^\infty p(\Delta u - \mu_{i,\hat{\mathbf{n}}}) \, p_\chi(\Delta u) \, d\Delta u$$

$$= c \sqrt{\frac{k_B T n_\xi^3}{8\pi m_0}} + \mathcal{O}(\mu_{i,\hat{\mathbf{n}}}) \equiv \Gamma(n_\xi, c) + \mathcal{O}(\mu_{i,\hat{\mathbf{n}}}). \quad (27)$$

Only the contribution of the zeroth order in $\mu_{i,\hat{\mathbf{n}}}$ is required, since the last term in Eq. (25) already contributes the required term linear in $\dot{\gamma}$ by setting $\mathbf{v}_i = \dot{\gamma} y_i \hat{\mathbf{x}}$. For the second necessary mean value, we obtain

TABLE I. Values of $|y_A|$ and $|\alpha_{\eta,\hat{\mathbf{n}}}|$ for all collision vectors $\hat{\mathbf{n}}$. Both quantities y_A and $\alpha_{\eta,\hat{\mathbf{n}}}$ have the same sign equal to $-\text{sign}(\hat{\mathbf{n}} \cdot \hat{\mathbf{y}})$ and only appear as product in Eq. (30). Furthermore, note that only collision vectors with $\hat{\mathbf{n}} \cdot \hat{\mathbf{x}} \neq 0$ are relevant for the evaluation of Eq. (30).

$\hat{\mathbf{n}}$	$|y_A|$	$|\alpha_{\eta,\hat{\mathbf{n}}}|$
$\hat{\mathbf{x}}, \hat{\mathbf{z}}, (\hat{\mathbf{x}} \pm \hat{\mathbf{z}})/\sqrt{2}$	0	0
$\hat{\mathbf{y}}$	1/4	1/2
$(\hat{\mathbf{x}} \pm \hat{\mathbf{y}})/\sqrt{2}, (\hat{\mathbf{y}} \pm \hat{\mathbf{z}})/\sqrt{2}$	1/6	1/3
$(\hat{\mathbf{x}} \pm \hat{\mathbf{y}} \pm \hat{\mathbf{z}})/\sqrt{3}$	13/96	13/48

$$\langle \chi(\Delta u)\Delta u \rangle = \int_0^\infty \Delta u\, p(\Delta u - \mu_{i,\hat{\mathbf{n}}})\, p_\chi(\Delta u)\, d\Delta u$$

$$= c\left(\frac{k_B T n_\xi}{2m_0} + \sqrt{\frac{k_B T n_\xi^3}{2\pi m_0}}\, \mu_{i,\hat{\mathbf{n}}} \right) + \mathcal{O}(\mu_{i,\hat{\mathbf{n}}}^2)$$

$$\equiv \Xi(n_\xi, c) + \Omega(n_\xi, c)\mu_{i,\hat{\mathbf{n}}} + \mathcal{O}(\mu_{i,\hat{\mathbf{n}}}^2) \qquad (28)$$

up to the linear order in $\mu_{i,\hat{\mathbf{n}}} \propto \dot{\gamma}$. One can show that the zeroth-order term $\Xi(n_\xi, c)$ does not contribute to σ_{xy}, as it should be. The contribution vanishes for collision planes with $y_A = 0$ or in combination with two collision vectors. Using Eqs. (27) and (28) in the expression (25) and only collecting all terms linear in $\dot{\gamma}$, we arrive at

$$\sigma_{xy} = \frac{m_0 \dot{\gamma}}{a_0^2 \Delta t\, n_\xi} \left\langle (\hat{\mathbf{x}} \cdot \hat{\mathbf{n}})^2 \sum_{y_i > y_0} y_i\, \Omega + (n_\xi - 1) \right.$$

$$\left. \times \left[y_i \Gamma + \text{sign}(\mathbf{x}_i \cdot \hat{\mathbf{n}})\, y_A \Omega \right] \right\rangle. \qquad (29)$$

Here, the remaining average $\langle \cdots \rangle$ goes over $\mathbf{x}_i$, the offset y_0 of the plane $P_{\hat{\mathbf{y}}, y_0}$, and the collision vector $\hat{\mathbf{n}}$.

As in the derivation of the equation of state, we replace the average over all particles and the conditional sum by a volume integral over $n_\xi / a_0^3\, \Theta(y - y_0)$ and also average over y_0. With only the average over the collision vector $\hat{\mathbf{n}}$ remaining, we obtain

$$\sigma_{xy} = \frac{m_0 \dot{\gamma}}{a_0^2 \Delta t} \left\langle (\hat{\mathbf{x}} \cdot \hat{\mathbf{n}})^2 \left\{ \Omega/12 + (n_\xi - 1)\left[\Gamma/12 + (\alpha_{\eta,\hat{\mathbf{n}}}\, y_A)\, \Omega \right] \right\} \right\rangle, \qquad (30)$$

where

$$\alpha_{\eta,\hat{\mathbf{n}}} \equiv \frac{1}{a_0^4} \int_{\mathcal{V}_\xi} \int_{-a_0/2}^{a_0/2} \text{sign}(\mathbf{x} \cdot \hat{\mathbf{n}})\Theta(y - y_0)\, dy_0\, dV. \qquad (31)$$

In Table I, we give the values $\alpha_{\eta,\hat{\mathbf{n}}}$ and y_A for all collision vectors $\hat{\mathbf{n}}$. Averaging over all of them, we obtain for the collisional viscosity without taking into account angular momentum conservation in the collision rule of Eq. (2),

$$\eta_{\text{coll}}^{-A} = \frac{m_0}{78\, a_0^2 \Delta t} \left\{ \frac{13}{6}\left[\Gamma(n_\xi - 1) + \Omega \right] + \frac{361}{576}\, \Omega(n_\xi - 1) \right\}. \qquad (32)$$

For our choice of $c = 1/100$ and $n_\xi = 20$, we obtain $\Omega \approx 5/14$ and $\Gamma = \Omega/2$. If instead of Eq. (4), we use Eq. (5) to have a bounded collision probability $p_\chi(\Delta u)$, we still can evaluate the averages of Eqs. (27) and (28) and expand into $\dot{\gamma}$. The resulting expressions for Ω and Γ are given in Appendix C. For $c = 1/100$ and $n_\xi = 20$, we then obtain $\Omega \approx 1/4$ and $\Gamma \approx 9/65$.

So far, we did not consider the term due to angular momentum conservation in our collision rule (2) when evaluating σ_{xy}. We follow here Ref. 45 to take into account two additional terms. The essential contribution is the rotational motion of the particles in the collision cell induced by the vorticity of the shear flow, which generates the rotational velocity $\boldsymbol{\omega} = \nabla \times \mathbf{v}/2 = -\dot{\gamma}/2\hat{\mathbf{z}}$. The velocity $\boldsymbol{\omega} \times \mathbf{x}_{i,c}$ of particle i due to this rotational flow is removed during the random collision, and we have to add it to $\mathbf{v}_i^{\text{new}} - \mathbf{v}_i$ considered so far to preserve angular momentum. More precisely, our collision rule (2)

only considers the component normal to the collision plane, and when we average over all collision vectors, we realize that only the x component of $\boldsymbol{\omega} \times \mathbf{x}_{i,c}$ is needed. Hence, in total, we need to add to the last term in Eq. (25) the normal velocity component $(\hat{\mathbf{n}} \cdot \hat{\mathbf{x}})\dot{\gamma} y_{ic}/2$. When averaging over all particle positions $j \neq i$, we can set $y_{i,c} = y_i - y_\xi = y_i(1 - 1/n_\xi)$ following a similar reasoning as in footnote 1. Thus, a careful inspection of Eq. (25) and the following steps show that we have to subtract half of the last term in Eq. (25). Ultimately, this replaces Γ in Eq. (32) by $\Gamma/2$.

A minor contribution comes from the random velocity changes δv_j during collision. We mention it here since it gives a near perfect agreement with the simulation results we will present in Fig. 5(a). The random changes δv_j add the angular momentum $\sum_j \mathbf{x}_{j,c} \times \hat{\mathbf{n}}\, \delta v_j$ to the cell, for which we have to subtract a term in the second line of Eq. (2) in order to restore angular momentum conservation. This velocity also has to be considered in $\hat{\mathbf{x}} \cdot (\mathbf{v}_i^{\text{new}} - \mathbf{v}_i)$ when starting with Eq. (24) for σ_{xy}, and then, the relevant steps carefully have to be repeated. As before, we only need the z component of the angular momentum. Dividing by the moment of inertia for the relevant z direction, $\mathbf{I}_{\xi,zz}/m_0 = \sum_j x_j^2 + y_j^2$, and taking the average over Δu, we obtain the mean angular velocity $\langle \omega_z^{\delta v_i} \rangle_{\Delta u} = \hat{\mathbf{x}} \cdot \hat{\mathbf{n}}\, \left\langle \chi(\Delta u) \frac{\sum_j y_{j,c}\Delta u/2\, \text{sign}(\mathbf{x}_j \cdot \hat{\mathbf{n}})}{\mathbf{I}_{\xi,zz}/m_0} \right\rangle$. Then, evaluating this average and introducing the mean moment of inertia $\langle \mathbf{I}_\xi \rangle_{zz}/m_0 = a_0^2(n_\xi - 1)/6$ gives $\langle \omega_z^{\delta v_i} \rangle_{\Delta u} = -12(\hat{\mathbf{x}} \cdot \hat{\mathbf{n}})^2 y_A^2 \dot{\gamma}\, \Omega/a_0^2$, where we neglected correlations in the product $y_j \Delta u$ and used $\langle \chi(\Delta u)\Delta u \rangle \simeq -2\Omega \hat{\mathbf{x}} \cdot \hat{\mathbf{n}} y_A \dot{\gamma}$. Finally, from the angular velocity, one calculates the mean x component of the velocity correction, $\langle \langle \omega_z^{\delta v_i} \rangle_{\Delta u} y_{ic} \rangle$. Performing the remaining averages, one ultimately realizes that this changes the prefactor of Ω in Eq. (32) from 361/567 to $0.5034 \approx 1/2$. Together with the correction from the previous paragraph, we then obtain the final formula for the shear viscosity,

$$\eta_{\text{coll}}^{+A} = \frac{m_0}{78\, a_0^2 \Delta t} \left\{ \frac{13}{6}\left[\frac{\Gamma}{2}(n_\xi - 1) + \Omega \right] + \frac{\Omega}{2}(n_\xi - 1) \right\}. \qquad (33)$$

B. Streaming viscosity

To determine the streaming viscosity based on the linear shear flow of Eq. (22), we follow the work of Kikuchi *et al.*[50] They determined the shear stress component σ_{xy} from the momentum along the x direction transported through the plane $y = 0$ during the streaming time Δt. They showed that this results in the expression

$$\sigma_{xy} = \frac{m_0 n_\xi}{a_0^3}\left(\frac{\dot{\gamma}\Delta t}{2}\langle v_y^2 \rangle - \langle v_x v_y \rangle \right), \qquad (34)$$

where v_x and v_y are velocity components of the fluid particles. The average is performed at the beginning of the streaming step. In the steady state, we can immediately use $\langle v_y^2 \rangle = k_B T/m_0$. However, as we explain now, the velocity correlation $\langle v_x v_y \rangle$ changes when we cycle once through the streaming and collision step. However, in the steady state, it should be back to the value at the start of the cycle. Using this self-consistency condition, one can ultimately determine $\langle v_x v_y \rangle$ and therefore σ_{xy}.

First of all, if $p(v_x, v_y)$ is the velocity distribution of the particles at the beginning of the streaming step, it will evolve toward

the distribution $p(v_x + \dot{\gamma}v_y\Delta t, v_y)$ at the end of the streaming step since particles in the shear flow acquire additional speed along the x axis when moving along the y direction. Based on this altered distribution, the velocity correlation at the end of the streaming step becomes[50]

$$\langle v_x v_y \rangle_{\text{str}}^{\text{new}} = \langle v_x v_y \rangle - \dot{\gamma}\Delta t \langle v_y^2 \rangle. \qquad (35)$$

In other words, the value of $\langle v_x v_y \rangle$ decreases by a constant value during the streaming step. Both Eqs. (34) and (35) are common to all MPCD algorithms.[45]

In a second step, $\langle v_x v_y \rangle_{\text{str}}^{\text{new}}$ is altered during the subsequent collision step. This depends on the detailed collision rule. As we demonstrate below and in Appendix D, the velocity correlations change by a constant factor during collision. Thus, $\langle v_x v_y \rangle_{\text{coll}}^{\text{new}} = (1 - b)\langle v_x v_y \rangle_{\text{str}}^{\text{new}}$. Inserting Eq. (35) and using the self-consistency condition $\langle v_x v_y \rangle_{\text{coll}}^{\text{new}} = \langle v_x v_y \rangle$ as explained above, we can solve

$$\langle v_x v_y \rangle = \left(1 - \frac{1}{b}\right)\dot{\gamma}\Delta t \langle v_y^2 \rangle. \qquad (36)$$

We insert this result into the expression (34) for σ_{xy} and use $\langle v_y^2 \rangle = k_B T/m_0$ to finally arrive at

$$\sigma_{xy} = \frac{\dot{\gamma}n_\xi k_B T \Delta t}{a_0^3}\left(\frac{1}{b} - \frac{1}{2}\right). \qquad (37)$$

Thus, after determining the factor $1 - b$ for our collision rule, we will have an expression for the streaming viscosity.

In order to write $\langle v_x v_y \rangle_{\text{coll}}^{\text{new}}$ in a compact way, we abbreviate in the collision rule of Eq. (2) the term added to restore angular momentum conservation by $\mathbf{A}$ and use for the other term $\mathbf{B}_i = \hat{\mathbf{n}}[\hat{\mathbf{n}} \cdot (\mathbf{v}_\xi - \mathbf{v}_i) + \delta v_i]$. Furthermore, right before the collision, the velocity correlation is $\langle v_x v_y \rangle_{\text{str}}^{\text{new}}$ so that we have

$$\begin{aligned}\langle v_x v_y \rangle_{\text{coll}}^{\text{new}} = {}& \langle v_x v_y \rangle_{\text{str}}^{\text{new}} \\ & + \langle \chi(\Delta u)[v_{i,x}B_{i,y} + B_{i,x}v_{i,y} + v_{i,x}A_y + A_x v_{i,y} \\ & + A_x A_y + B_{i,x}B_{i,y} + A_x B_{i,y} + A_y B_{i,x}]\rangle.\end{aligned} \qquad (38)$$

Since the value of $\chi(\Delta u)$ is either 0 or 1, we have set $\chi(\Delta u)^2 = \chi(\Delta u)$. Note that in $\delta v_i = \delta v_i^s + \delta v_i^t$, we can drop δv_i^s since it is zero, on average, and also set $\delta v_t = \bar{v}_{B/A}$ using $n_A = n_B \approx n_\xi/2$ in Eq. (7). Hence, we will always use $\delta v_i = \bar{v}_{B/A}$ in the following. For the first term in Eq. (38), we demonstrate here how it is evaluated and refer to Appendix D for the evaluation of all the other terms. We obtain with $\delta v_i = \bar{v}_{B/A}$

$$\langle \chi(\Delta u)v_{i,x}B_{i,y} \rangle = \langle \chi(\Delta u)v_{i,x}n_y[\bar{v}_{B/A} + \hat{\mathbf{n}} \cdot (\mathbf{v}_\xi - \mathbf{v}_i)]\rangle.$$

Here, we recognize that $\bar{v}_{B/A} + \hat{\mathbf{n}} \cdot \mathbf{v}_\xi = 2/n_\xi \sum_{\{j \in \mathscr{V}_{B/A}\}} \hat{\mathbf{n}} \cdot \mathbf{v}_j$ after using the respective definitions of $\bar{v}_{B/A}$ and $\mathbf{v}_\xi$. Since the construction particles i and j lie on different sides of the collision plane and are therefore different, this term vanishes under the typical molecular chaos assumption $\langle v_{i,x}v_{j,y} \rangle = 0$. For the remaining term, we realize that it involves the projector $\hat{\mathbf{n}} \otimes \hat{\mathbf{n}}$, which when averaging over all $\hat{\mathbf{n}}$ gives the unit matrix $\mathbf{1}/3$. Hence, we ultimately have

$$\begin{aligned}\langle \chi(\Delta u)v_{i,x}B_{i,y} \rangle &= -\langle \chi(\Delta u)v_{i,x}v_{i,y} \rangle/3. \\ &\approx -\langle \chi(\Delta u) \rangle\langle v_{i,x}v_{i,y} \rangle/3. \end{aligned} \qquad (39)$$

In the last line, we used again the molecular chaos assumption and neglected higher correlations for particle i.

For the derivation of the remaining terms in Eq. (38), we refer to Appendix D. Finally, putting all terms in Eqs. (39), (D3), (D1), (D4), and (D8) into Eq. (38), we obtain

$$\langle v_x v_y \rangle_{\text{coll}}^{\text{new}} = \langle v_x v_y \rangle_{\text{str}}^{\text{new}}\left[1 - \langle \chi(\Delta u) \rangle \frac{14 - 13n_\xi + 8n_\xi^2}{18n_\xi^2}\right], \qquad (40)$$

from which we read off the factor b as the second term in the brackets. Using it in Eq. (37) together with $\langle \chi(\Delta u) \rangle \approx \Gamma(n_\xi, c)$ from Eq. (27) and dividing by the shear rate, we obtain the streaming viscosity

$$\eta_{\text{str}} = \frac{n_\xi k_B T \Delta t}{a_0^3}\left[\frac{18n_\xi^2}{(14 - 13n_\xi + 8n_\xi^2)\Gamma(n_\xi, c)} - \frac{1}{2}\right]. \qquad (41)$$

The sum of this equation and the collisional viscosity from Eq. (33) gives the complete shear viscosity in this new version of MPCD,

$$\eta = \eta_{\text{str}} + \eta_{\text{coll}}^{+A}. \qquad (42)$$

V. COMPARISON WITH SIMULATIONS

In this section, we compare the derived analytic expressions (21) for the pressure and (33) and (41) for the collision and streaming viscosities with values obtained from simulations. To calculate the collisional contribution to the pressure, we use with Eq. (11) the same formula with which we started the analytic calculations. Likewise, for the collisional and streaming viscosities, we set up the linear shear–flow profile $\mathbf{v}(y) = \dot{\gamma}y\hat{\mathbf{x}}$ and then explore Eqs. (24) and (34), respectively, to evaluate the viscosities from $\eta = \sigma_{xy}/\dot{\gamma}$. Finally, to test our method in a realistic situation, we also simulate a Poiseuille flow profile and measure the total viscosity from the maximum flow velocity. We start with some computational details.

A. Computational details

To calculate the collisional contribution to the pressure equation of state, we perform MPCD simulations in a box with edge length L using periodic boundary conditions and the parameters introduced further below. The setups of the shear flow profile and the Poiseuille flow need more comments. All the simulations are performed with the bounded collision probability of Eq. (5). For the pressure, we will also show results for the alternative form of Eq. (6).

1. Linear shear flow profile

To generate a steady shear flow profile with constant shear rate $\partial_y v_x = \dot{\gamma}$ in a cubic simulation box with edge length L, we use the so-called Lees–Edwards boundary conditions. We introduce them shortly.[50,52] In the directions along the $\hat{\mathbf{x}}$ and $\hat{\mathbf{z}}$ axes, perpendicular to the shear gradient, regular periodic boundary conditions are applied. However, along the direction of the shear gradient, the boundary conditions are modified such that the periodic images of the system move with velocity $\pm L\dot{\gamma}$. This means that a particle receives a

shift in position and velocity when crossing the boundaries along the y direction. If the particle crosses the lower boundary at time t and position $(x, y = -L/2, z)$, it re-enters the system at the upper boundary at position $((x + L\dot\gamma t)_{\mathrm{mod}\,L}, y = +L/2, z)$ with velocity $(v_x + L\dot\gamma, v_y, v_z)$. If it crosses the corresponding upper boundary at time t and position $(x, y = +L/2, z)$, it re-enters the system at the lower boundary at position $((x - L\dot\gamma t)_{\mathrm{mod}\,L}, y = -L/2, z)$ with velocity $(v_x - L\dot\gamma, v_y, v_z)$.

2. Poiseuille flow profile

To generate a Poiseuille flow profile, we do not introduce bounding walls but simulate a driven system with periodic boundaries in all three dimensions and two profiles with opposing flow directions along the $\hat{x}$ axis.[53] For this, we introduce a pressure difference Δp by acting with a constant body force on all the particles. Particles with positions $y_i < 0$ experience the force $-m_0 g\hat{x}$, and for particles with positions $y_i > 0$, the force points in the opposite direction, $m_0 g\hat{x}$. This setup with the box dimensions $L \times 2L \times L$ produces two opposing Poiseuille flow profiles and thereby avoids the implementation of any solid boundaries. With the resulting pressure gradient $\Delta p/L = m_0 n_0 g/a_0^3$, the viscosity then follows from the maximum flow velocity $v_{\mathrm{max}} = \frac{\Delta p L}{8\eta}$.[54]

3. Parameters

For all simulations, we use the edge length $L = 64a_0$, the collision parameter $c = 1/100$, and, in MPCD units, set $k_B T = 1$ and mass $m_0 = 1$. For the Lees–Edwards simulations, the shear rate is chosen as $\dot\gamma = \partial_y v_x = 0.006\,25$ in units of the inverse MPCD time scale $t_0 = a_0\sqrt{m_0/k_B T}$.

Each system is initialized by randomly distributing $N = n_0 L^3$ particles in the volume L^3 and by choosing their velocities from the Maxwell–Boltzmann distribution. For the Lees–Edwards simulations, a local offset for the mean velocity component along the x direction is chosen, $\langle v_x \rangle = \dot\gamma y$. To equilibrate the system at the beginning, we simulate it for 10^5 time steps Δt. Then, we sample Eqs. (11), (24), and (34) during a simulation time of $5 \times 10^5 \Delta t$. When simulating the Poiseuille flow, we average the flow profile over the same amount of time but use an increased equilibration time of $5 \times 10^5 \Delta t$ to assure that the flow has reached its maximum velocity.

Our goal is to perform the MPCD simulations with defined values of the parameters, which we keep constant throughout the simulations. The collision parameter c introduced in Eq. (4) has to be sufficiently small so that we can explore the dependence on Δu, n_A, and n_B. It turns out that $c = 1/100$ and an average number of $n_0 = 20$ particles per cell is a suitable choice, which yields a collision rate of $\langle\chi(\Delta u)\rangle \approx 0.14$.

Together with a time step of $\Delta t = t_0/200$, our set of parameters is particularly interesting because it yields a total viscosity $\eta = \eta_{\mathrm{str}} + \eta_{\mathrm{coll}}^{+A} \approx 16a_0\sqrt{k_B T/m_0}$, which is commonly used for simulating microswimmers with MPCD.[8,9,12,17] Hence, in the following, we focus on densities between $n_0 = 7$ and $n_0 = 35$ and investigate how pressure and viscosities behave in this range of densities centered around $n_0 = 20$.

B. Equation of state

Figure 4 shows the simulated total pressure P, normalized by the ideal gas pressure $P_{\mathrm{id}} = n_0 k_B T/a_0^3$, as a function of density n_0 for
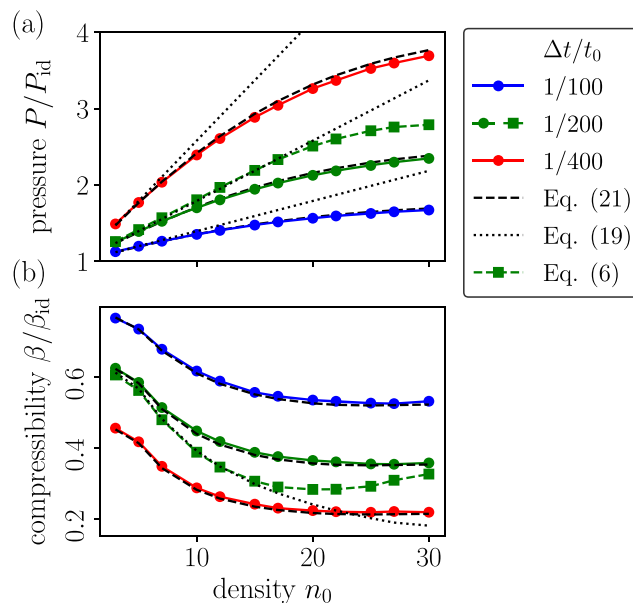

FIG. 4. (a) Total pressure P relative to the ideal gas pressure $P_{\mathrm{id}} = n_0 k_B T/a_0^3$ plotted vs density n_0 for three different values of the time step Δt. Circle symbols show data points obtained from simulations using Eq. (11) together with the bounded collision probability of Eq. (5), and dashed lines show the corresponding theory curves from Eq. (21). The dotted lines show the theory curves from Eq. (19), and the squares show data points obtained from simulations using the bounded collision probability of Eq. (6) for $\Delta t = t_0/200$. (b) The corresponding compressibility β relative to the ideal gas value $\beta_{\mathrm{id}} = a_0^3/(n_\xi k_B T)$ plotted vs n_0.

different time steps Δt. The colored circle symbols are the numerical results using the bounded collision probability from Eq. (5). They are in very good agreement with the analytic result of Eq. (21) plotted as dashed lines. In particular, the simulations confirm the relation $P_{\mathrm{coll}} \propto 1/\Delta t$ according to which a smaller Δt results in a larger pressure. This makes sense since the collision probability is independent of the time step Δt. Hence, there are more collisions in the same time interval when Δt decreases. As dotted lines, we also show the pressure of Eq. (19) calculated with the unbounded collision probability of Eq. (4). They are in very good agreement with the simulated pressure only until $\sim n_0 = 10$. With the idea to enhance the pressure in the simulations further, we also used the alternative bounded collision probability of Eq. (6). Indeed, for the example of $\Delta t = t_0/200$, we obtain a larger pressure (square symbols) since we keep the linear dependence in $\Delta u n_A n_B$ until the probability becomes one. It starts to deviate from the dotted line not until $n_0 = 20$.

In Fig. 4(b), we plot the corresponding compressibility as a function of n_0 relative to its ideal-gas value $\beta_{\mathrm{id}} = 1/P_{\mathrm{id}}$. Using $P = P_{\mathrm{id}}[1 + f(n_0)]$, the compressibility

$$\beta = \frac{1}{n_0}\left(\frac{\partial P}{\partial n_0}\right)^{-1} = \beta_{\mathrm{id}}\frac{1}{1 + f + \frac{\partial f}{\partial n_0}} \qquad (43)$$

can be directly related to the deviation of pressure from P_{id}. The dashed and dotted lines in Fig. 4(b) represent the analytic results calculated from the formulas for pressure, while the derivative $\partial f/\partial n_0$

for the numerical results was determined with the standard Python toolchain. Relative to the ideal-gas value, compressibility is further reduced and, in particular, β also decreases with the decrease in Δt. For example, at $\Delta t = t_0/200$ and with $n_0 = 20$ as a reasonable density, compressibility is reduced to $0.4\beta_{id}$. Now, applying the bounded collision probability of Eq. (6), the compressibility is down to $0.3\beta_{id}$. To obtain such a reduction with conventional MPCD methods and the ideal-gas pressure, one would need to increase the particle number per cell by a factor of three. Thus, the new collision rule with its non-ideal equation of state reduces the computational efforts.

C. Shear viscosity

We first discuss the collisional viscosity. Figure 5(a) shows the simulated collisional viscosity η_{coll}^{+A} in MPCD units $m_0/(a_0 t_0)$ as a function of the density n_0 for three values of Δt. The circle symbols show data points from simulations using the bounded collision rule Eq. (5). Over a wide range of densities, the values are in very good agreement with the analytical result of Eq. (33) shown as dashed lines. Hence, there is a quantitative agreement between simulations and theory. Similar to the pressure, the simulations confirm the scaling $\eta_{coll}^{+A} \propto 1/\Delta t$. For the two larger time steps $\Delta t = t_0/100 \Delta t = t_0/200$, we see a deviation at densities $n_0 \leq 10$. We attribute this to the following reasons: first, our collision rule is not constructed for small numbers of particles, and second, to derive Eq. (33), we neglected

fluctuations of the center of mass position, which also requires a higher number of particles.

We now continue with the streaming viscosity η_{str} that we extract from the same simulations. Figure 5(b) shows η_{str} in MPCD units $m_0/(a_0 t_0)$ as a function of the density n_0 and for different values of Δt. Again, the circle symbols show data points for the bounded collision rule from Eq. (5), while dotted lines refer to the analytic values given by Eq. (41). Although we observe an approximate quantitative agreement of the simulated values for η_{str} with Eq. (41) for larger densities n_0, there are clear differences. First, Eq. (41) predicts an increase in the streaming viscosity toward smaller n_0, which then falls sharply to zero at $n_0 = 0$ (not shown). The simulated streaming viscosities only show a slight increase for $\Delta t = t_0/100$; otherwise, they are roughly independent of n_0. Second, while we do not reproduce the predicted scaling $\eta_{str} \propto \Delta t$, we observe a clear increase in the streaming viscosity with Δt, and thus, the expected trend is reproduced qualitatively. As a main reason for the disagreement of the simulated viscosities with Eq. (41), we consider the approximation $\langle \chi(\Delta u) v_{i,x} v_{i,y} \rangle \approx \langle \chi(\Delta u) \rangle \langle v_{i,x} v_{i,y} \rangle$ made during the derivation of Eq. (41). Nevertheless, factoring out the collision rate $\langle \chi(\Delta u) \rangle$ in the previous expression provides a rough quantitative estimate of the streaming viscosity η_{str} as demonstrated.
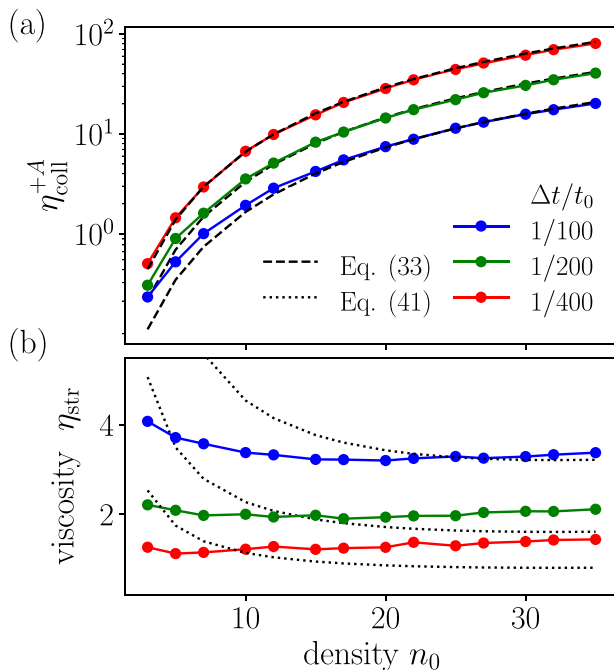

FIG. 5. (a) Collisional viscosity η_{coll}^{+A} in MPCD units $m_0/(a_0 t_0)$ plotted vs density n_0 for three values of the time step Δt. Circle symbols show data points obtained from simulations using Eq. (24), and the dashed lines show the corresponding analytical values as given by Eq. (33). (b) Streaming viscosity η_{str} in MPCD units $m_0/(a_0 t_0)$ plotted vs density n_0 for the same values of Δt. Here, the circle symbols show data points obtained from the same simulations using Eq. (34), and the dotted lines refer to the analytic expression of Eq. (41).
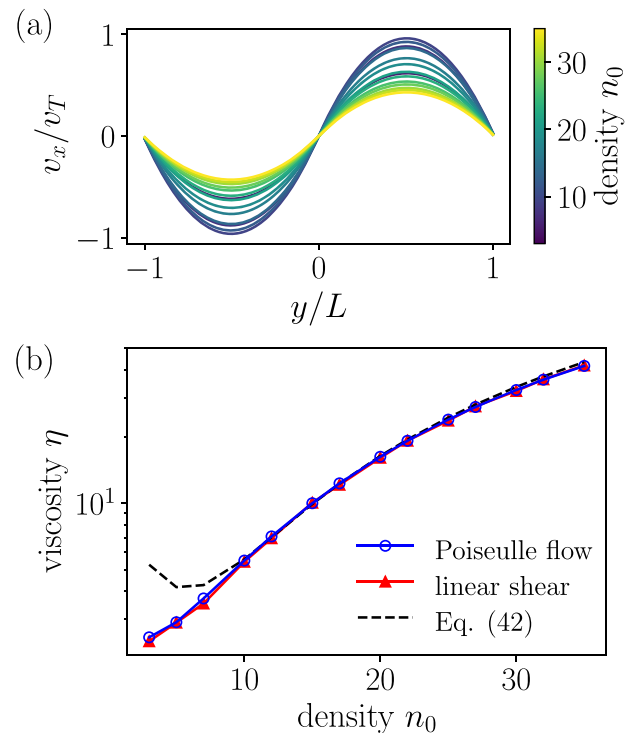

FIG. 6. (a) Poiseuille flow profiles v_x vs lateral channel position y determined in simulations for different densities n_0. The velocity unit is the thermal velocity $v_T = \sqrt{k_B T/m_0}$. (b) Total viscosity in MPCD units $m_0/a_0 t_0$. Blue circle symbols show data points for the viscosity determined from the flow profiles in (a). The red triangle symbols refer to data points resulting from the sum of viscosities, $\eta_{str} + \eta_{coll}^{+A}$, determined in Sec. V C. The black dashed line shows the analytical expression of Eq. (42).

D. Poiseuille flow

To simulate the Poiseuille flow profiles, we used the time step $\Delta t = t_0/200$. After averaging the velocity field over the time $5 \times 10^4 \Delta t$, the final flow profiles are generated by also averaging along the x and z directions. The resulting profiles v_x as a function of the y position are shown in Fig. 6(a) for different densities n_0. The two opposing profiles are clearly visible, and in both regions $y < 0$ and $y > 0$, we observe excellent agreement with the expected parabolic shape. The decrease in the flow velocity toward higher densities n_0 already indicates an increase in the total viscosity η with n_0. This increase is even more pronounced since also the pressure difference Δp increases with n_0 because we always use the same body force per fluid particle.

In Fig. 6(b), we plot the total viscosity η as a function of the density n_0. The blue circle symbols show data points obtained by extracting v_{max} from the Poiseuille flow profiles shown in Fig. 6(a) and using $\eta = \Delta p L/(8 v_{max})$. The red triangle symbols show the total viscosity $\eta_{coll}^{+A} + \eta_{str}$ consisting of the collisional and streaming viscosity, which we determined in Sec. V C from the simulated linear shear profile. The numerical data are compared to the analytical result of Eq. (42), which is shown as the dashed line.

First of all, the values for the viscosities, determined in the simulations by analyzing either momentum transfer in linear shear flow or the maximum flow speed of the Poiseuille profile, are in excellent agreement over the whole range of densities. In addition, we also observe a good agreement with the analytical expression of Eq. (42) for densities $n_0 \geq 10$, where the collisional viscosity η_{coll}^{+A} dominates. For low densities $n_0 < 10$, the deviations occur due to η_{str} as discussed before.

VI. CONCLUSIONS AND OUTLOOK

The new collision rule in our extended MPCD method provides the fluid with a non-ideal equation of state by introducing stochastic collisions between two particle clouds in the collision cell. In short, the collision frequency is quadratic in density and collisions only occur if the particle clouds move toward each other. In contrast to prior approaches, the extended MPCD method is designed for three dimensions, conserves angular momentum, and features a thermostat. The main goal of our method is to guarantee a low fluid compressibility for simulations in which significant pressure gradients occur. Since with the reduced compressibility, we can keep the particle number per collision cell at reasonably small values, our method requires significantly less simulation time compared to raising the fluid density in classical MPCD algorithms.[12] We provide an example in footnote.[55] At the same time, our method saves computer memory necessary to store MPCD particles so that we do not need to reduce the system size. We will explore this more in a planned second publication.

Based on the new collision rule, we have derived the equation of state and also demonstrated the impact of different collision probabilities. Indeed, in the regime where the collision probability is quadratic in density, we observe the nonlinear quadratic variation of pressure with density. For larger densities, where the collision frequency is bounded by the maximum value $1/\Delta t$, the pressure again becomes linear in density, albeit at a higher value, which

increases with $1/\Delta t$. For typical values of $\Delta t/t_0 = 1/200$ and $n_0 = 20$ together with the most effective collision probability, compressibility is reduced by a factor three compared to the ideal-gas value at $n_0 = 20$. Overall, we find very good agreement with values obtained from simulations in the regime where our analytic expressions apply.

Moreover, for the shear viscosity, we have derived analytic expressions for the contributions of the collision and streaming step. For the collisional viscosity, we find very good agreement with the values obtained from simulating a linear shear flow and determining momentum transport, while for the streaming viscosity, the analytic expression only provides a rough estimate. However, for density values n_0 above 10, the collisional viscosity starts to dominate and we obtain a very good agreement with the simulated values. This is also demonstrated by simulating a Poiseuille flow and extracting viscosity from the maximum flow velocity.

In a planned second publication, we will use our extended MPCD method for selected flow problems to demonstrate its applicability. Furthermore, we intend to apply it to dense systems of microswimmers, where large pressure fields arise naturally. Preliminary simulations of such systems show that the extended MPCD method keeps the inhomogeneities in fluid density small. This will help us to obtain reliable insight into how hydrodynamic flow fields influence the collective dynamics of clustering and swarming microswimmers.

APPENDIX A: GAUSSIAN DISTRIBUTION FOR Δu

For the derivation of the pressure, the fluid is considered at rest. Assuming molecular chaos, the velocities $\mathbf{v}_j$ of the individual particles all obey the Maxwell–Boltzmann distribution. For the scalar product with the collision vector $\hat{\mathbf{n}}$, this implies the probability density

$$p(\mathbf{v}_j \cdot \hat{\mathbf{n}}) = \sqrt{\frac{m_0}{2\pi k_B T}} \exp\left(-\frac{m_0 (\mathbf{v}_j \cdot \hat{\mathbf{n}})^2}{2 k_B T}\right). \tag{A1}$$

The probability distribution for $\Delta u = \bar{v}_B - \bar{v}_A$ then follows from

$$p(\Delta u) = \int \delta\left(\Delta u - \left[\sum_{\{\mathbf{x}_j \in \mathscr{V}_B\}} \frac{\mathbf{v}_j \cdot \hat{\mathbf{n}}}{n_B} - \sum_{\{\mathbf{x}_j \in \mathscr{V}_A\}} \frac{\mathbf{v}_j \cdot \hat{\mathbf{n}}}{n_A}\right]\right)$$
$$\times \prod_{j=1}^{N} p(\mathbf{v}_j \cdot \hat{\mathbf{n}}) d(\mathbf{v}_j \cdot \hat{\mathbf{n}}), \tag{A2}$$

where $\delta(\cdots)$ stands for the delta function. Eliminating it by integrating over one normal velocity component and then carefully performing the rest of the $N - 1$ integration finally gives the Gaussian distribution

$$p(\Delta u) = \frac{1}{\sqrt{2\pi\langle\Delta u^2\rangle}}\exp\left(-\frac{\Delta u^2}{2\langle\Delta u^2\rangle}\right). \tag{A3}$$

It has zero mean, $\langle\Delta u\rangle = 0$, and variance

$$\langle\Delta u^2\rangle = \frac{k_B T}{n_A m_0} + \frac{k_B T}{n_B m_0} = \frac{4 k_B T}{m_0 n_\xi}, \tag{A4}$$

where we used the approximation $n_{A/B} \approx n_\xi/2$ in the last step. Thus, the sum over Gaussian distributed random numbers follows again a Gaussian distribution.

APPENDIX B: CONDITIONAL DISTRIBUTION OF Δu IN SHEAR FLOW

For deriving the collisional shear viscosity in Sec. IV A, we need the distribution for Δu under the condition that the collision vector $\hat{\mathbf{n}}$ and the position $\mathbf{x}_i$ of particle i are given. We again start with the single-particle velocity distributions. Relative to the applied shear flow, the velocities still follow the Maxwell–Boltzmann distribution,

$$p(\mathbf{v}_j \cdot \hat{\mathbf{n}}, y_j) = \sqrt{\frac{m_0}{2\pi k_B T}}\exp\left(-\frac{m_0\left[(\mathbf{v}_j - \dot{\gamma} y_j \hat{\mathbf{x}})\cdot\hat{\mathbf{n}}\right]^2}{2 k_B T}\right). \tag{B1}$$

Following the same reasoning as in Appendix A, this implies that the conditional distribution for Δu is again Gaussian with the same variance as before: $\langle(\Delta u - \langle\Delta u\rangle)^2\rangle = 4 k_B T/(m_0 n_\xi)$.

However, the conditional mean of Δu under the applied shear flow and for fixed $\hat{\mathbf{n}}$ and $\mathbf{x}_i$ is non-zero. Starting from the definition of Δu and averaging over all particle velocities and all positions besides particle i, one obtains

$$\langle\Delta u\rangle_{i,\hat{\mathbf{n}}} = \dot{\gamma}\hat{\mathbf{x}}\cdot\hat{\mathbf{n}}\left[\sum_{\{\mathbf{x}_j\in\mathscr{V}_B/\mathbf{x}_i\}}\frac{\langle y_j\rangle}{n_B} - \sum_{\{\mathbf{x}_j\in\mathscr{V}_A/\mathbf{x}_i\}}\frac{\langle y_j\rangle}{n_A}\right] - \mathrm{sign}(\mathbf{x}_i\cdot\hat{\mathbf{n}})\frac{y_i}{n_{A/B}}, \tag{B2}$$

where the subscripts $i, \hat{\mathbf{n}}$ indicate the conditions that the particle i resides at $\mathbf{x}_i$ and the collision vector takes the value $\hat{\mathbf{n}}$. When we introduce the center-of-mass in the respective regions $\langle y_j\rangle = y_{A/B}$ for $\mathbf{x}_j \in \mathscr{V}_{A/B}$ and use $y_A = -y_B$ and $n_{A/B} \approx n_\xi/2$, we can ultimately write the conditional mean as

$$\langle\Delta u\rangle_{i,\hat{\mathbf{n}}} = -2\dot{\gamma}\hat{\mathbf{x}}\cdot\hat{\mathbf{n}}\frac{y_A(n_\xi - 1) + \mathrm{sign}(\mathbf{x}_i\cdot\hat{\mathbf{n}})\,y_i}{n_\xi} \equiv \mu_{i,\hat{\mathbf{n}}}. \tag{B3}$$

Based on the conditional distribution $p(\Delta u - \mu_{i,\hat{\mathbf{n}}})$, we can now calculate the required mean values $\langle\chi(\Delta u)\rangle$ and $\langle\chi(\Delta u)\Delta u\rangle$ in shear flow.

APPENDIX C: MEAN VALUES $\langle\chi(\Delta u)\rangle$ AND $\langle\chi(\Delta u)\Delta u\rangle$ IN SHEAR FLOW

We start with the unbounded form of the collision rate $p_\chi(\Delta u)$ in Eq. (4) and find for the mean collision rate

$$\begin{aligned}
\langle\chi(\Delta u)\rangle &= \int_0^\infty p(\Delta u - \mu_{\mathbf{x}_i,\hat{\mathbf{n}}})\,p_\chi(\Delta u)\,\mathrm{d}\Delta u \\
&= \frac{c n_\xi}{2}\left\{\sqrt{\frac{k_B T n_\xi}{2\pi m_0}}\exp\left(-\frac{\mu_{i,\hat{\mathbf{n}}}^2 m_0 n_\xi}{4 k_B T}\right)\right. \\
&\quad \left. + \frac{\mu_{i,\hat{\mathbf{n}}} n_\xi}{8}\left[1 + \mathrm{erf}\left(\mu_{i,\hat{\mathbf{n}}}\sqrt{\frac{m_0 n_\xi}{8 k_B T}}\right)\right]\right\} \\
&= c\sqrt{\frac{k_B T n_\xi^3}{8\pi m_0}} + \mathscr{O}(\mu_{i,\hat{\mathbf{n}}}) \equiv \Gamma(n_\xi, c) + \mathscr{O}(\mu_{i,\hat{\mathbf{n}}}),
\end{aligned} \tag{C1, C2}$$

where in the last line, we show the relevant zeroth-order term after expansion in $\mu_{i,\hat{\mathbf{n}}}$. For the second mean value, we obtain

$$\begin{aligned}
\langle\chi(\Delta u)\Delta u\rangle &= \int_0^\infty \Delta u\,p(\Delta u - \mu_{\mathbf{x}_i,\hat{\mathbf{n}}})\,p_\chi(\Delta u)\,\mathrm{d}\Delta u \\
&= \frac{c n_\xi}{2}\left\{\left(\frac{k_B T}{m_0} + \frac{\mu_{i,\hat{\mathbf{n}}}^2 n_\xi}{4}\right)\left[1 + \mathrm{erf}\left(\mu_{i,\hat{\mathbf{n}}}\sqrt{\frac{m_0 n}{8 k_B T}}\right)\right]\right. \\
&\quad \left. + \mu_{i,\hat{\mathbf{n}}}\sqrt{\frac{k_B T n_\xi}{2\pi m_0}}\exp\left(-\frac{\mu_{i,\hat{\mathbf{n}}}^2 m_0 n_\xi}{8 k_B T}\right)\right\}
\end{aligned} \tag{C3}$$

and, after expanding to first order in $\mu_{i,\hat{\mathbf{n}}}$,

$$\begin{aligned}
\langle\chi(\Delta u)\Delta u\rangle &= c\left(\frac{k_B T n_\xi}{2 m_0} + \sqrt{\frac{k_B T n_\xi^3}{2\pi m_0}}\,\mu_{i,\hat{\mathbf{n}}}\right) + \mathscr{O}(\mu_{i,\hat{\mathbf{n}}}^2) \\
&\equiv \Xi(n_\xi, c) + \Omega(n_\xi, c)\mu_{i,\hat{\mathbf{n}}} + \mathscr{O}(\mu_{i,\hat{\mathbf{n}}}^2).
\end{aligned} \tag{C4}$$

For the bounded form of the collision rate $p_\chi(\Delta u)$ in Eq. (5), we can also calculate the mean values. The mean collision rate becomes

$$\begin{aligned}
\langle\chi(\Delta u)\rangle &= \int_0^\infty p(\Delta u - \mu_{\mathbf{x}_i,\hat{\mathbf{n}}})\,p_\chi(\Delta u)\,\mathrm{d}\Delta u \\
&= \frac{1}{2}\left\{1 + \mathrm{erf}\left(\mu_{i,\hat{\mathbf{n}}}\sqrt{\frac{m_0 n_\xi}{8 k_B T}}\right)\right. \\
&\quad - \exp\left[\frac{c n_\xi^2}{8}\left(c n_\xi\frac{k_B T}{m_0} - 2\mu_{i,\hat{\mathbf{n}}}\right)\right] \\
&\quad \left. \times \mathrm{erfc}\left[\sqrt{\frac{n_\xi}{8}}\left(c n_\xi\sqrt{\frac{k_B T}{m_0}} - \mu_{i,\hat{\mathbf{n}}}\sqrt{\frac{m_0}{k_B T}}\right)\right]\right\} \\
&= 1 - \exp\left(\frac{c^2 k_B T n_\xi}{8 m_0}\right)\mathrm{erfc}\left(c\sqrt{\frac{k_B T n_\xi^3}{8 m_0}}\right) + \mathscr{O}(\mu_{i,\hat{\mathbf{n}}}) \\
&\equiv \Gamma(n_\xi, c) + \mathscr{O}(\mu_{i,\hat{\mathbf{n}}}^2),
\end{aligned} \tag{C5, C6}$$

where the last line shows the relevant zeroth-order term after expansion in $\mu_{i,\hat{\mathbf{n}}}$. The second mean value becomes

$$\langle \chi(\Delta u)\Delta u\rangle = \int_0^\infty \Delta u\, p(\Delta u - \mu_{\mathbf{x}_i,\hat{\mathbf{n}}})\, p_\chi(\Delta u)\, d\Delta u$$

$$= \frac{1}{2}\left\{ \mu_{i,\hat{\mathbf{n}}}\left[1 + \mathrm{erf}\left(\mu_{i,\hat{\mathbf{n}}}\sqrt{\frac{m_0 n_\xi}{8 k_\mathrm{B} T}}\right)\right]\right.$$

$$+ \left(c n_\xi \frac{k_\mathrm{B} T}{m_0} - \mu_{i,\hat{\mathbf{n}}}\right)$$

$$\times \exp\left[\frac{c n_\xi^2}{8}\left(c n_\xi \frac{k_\mathrm{B} T}{m_0} - 2\mu_{i,\hat{\mathbf{n}}}\right)\right]$$

$$\left.\times \mathrm{erfc}\left[\sqrt{\frac{n_\xi}{8}}\left(c n_\xi \sqrt{\frac{k_\mathrm{B} T}{m_0}} - \mu_{i,\hat{\mathbf{n}}}\sqrt{\frac{m_0}{k_\mathrm{B} T}}\right)\right]\right\},$$

and after expanding to first order in $\mu_{i,\hat{\mathbf{n}}}$, one has

$$\langle \chi(\Delta u)\Delta u\rangle = \frac{c k_\mathrm{B} T n_\xi}{2 m_0}\exp\left(c^2 \frac{k_\mathrm{B} T n_\xi^3}{8 m_0}\right)\mathrm{erfc}\left(c\sqrt{\frac{k_\mathrm{B} T n_\xi}{8 m_0}}\right)$$

$$+ \frac{\mu_{i,\hat{\mathbf{n}}}}{2}\left[1 + c\sqrt{\frac{k_\mathrm{B} T n_\xi^3}{2\pi m_0}} - \left(1 + c^2 \frac{k_\mathrm{B} T n_\xi^3}{4 m_0}\right)\right.$$

$$\left.\times \exp\left(c^2 \frac{k_\mathrm{B} T n_\xi^3}{8 m_0}\right)\mathrm{erfc}\left(c\sqrt{\frac{k_\mathrm{B} T n_\xi^3}{8 m_0}}\right)\right] + \mathcal{O}(\mu_{i,\hat{\mathbf{n}}}^2)$$

$$\equiv \Xi(n_\xi,c) + \Omega(n_\xi,c)\mu_{i,\hat{\mathbf{n}}} + \mathcal{O}(\mu_{i,\hat{\mathbf{n}}}^2). \tag{C7}$$

APPENDIX D: VELOCITY CORRELATION DURING COLLISIONS

To derive of the streaming viscosity in Sec. IV B, we consider the evolution of the velocity correlation $\langle v_{i,x}v_{i,y}\rangle_\mathrm{coll}^\mathrm{new}$ during a collision step. In the main text, we have already evaluated the term $\langle \chi(\Delta u)v_{i,x}B_{i,y}\rangle$. Here, we calculate the remaining terms $\langle \chi(\Delta u)v_x A_y\rangle$, $\langle \chi(\Delta u)A_x A_y\rangle$, $\langle \chi(\Delta u)B_{i,x}B_{i,y}\rangle$, and $\langle \chi(\Delta u)A_x B_{i,y}\rangle$.

We begin by applying some transformations on the abbreviations $\mathbf{B}_i$ and $\mathbf{A}$ that we introduced to write Eq. (38) in a compact way. First, we note that we may drop the stochastic part δv_i^s of $\delta v_i = \delta v_i^t + \delta v_i^s$ because it averages to zero. Furthermore, we replace $\delta v_i^t = \bar{v}_{A/B}$ using $n_A = n_B \approx n_\xi/2$. With the definitions of $\mathbf{v}_\xi$ and $\bar{v}_{A/B}$, the quantity $\mathbf{B}_i$ reads

$$\mathbf{B}_i = -\hat{\mathbf{n}}\cdot\mathbf{v}_i + \frac{2\hat{\mathbf{n}}}{n_\xi}\sum_{\{j\in\mathscr{V}_{B/A}\}}\hat{\mathbf{n}}\cdot\mathbf{v}_j.$$

Furthermore, we can insert the quantity $\mathbf{B}_j$ into $\mathbf{A}$,

$$\mathbf{A} \equiv -\mathbf{I}_\xi^{-1} m_0 \sum_{\mathbf{x}_{j,c}\in\mathscr{V}_\xi}\left[\mathbf{x}_{j,c}\times\hat{\mathbf{n}}\left(\delta v_j - \hat{\mathbf{n}}\cdot\mathbf{v}_j\right)\right]\times\mathbf{x}_{i,c}$$

$$= -\mathbf{I}_\xi^{-1} m_0 \sum_{\mathbf{x}_{j,c}\in\mathscr{V}_\xi}\left(\mathbf{x}_{j,c}\times\mathbf{B}_j\right)\times\mathbf{x}_{i,c},$$

and using that, we are free to add the constant velocity $\mathbf{v}_\xi$ inside the round brackets.

With these simplifications, we now begin considering the next most simple term $\langle \chi(\Delta u)B_{i,x}B_{i,y}\rangle$ of the new velocity correlation $\langle v_{i,x}v_{i,y}\rangle_\mathrm{coll}^\mathrm{new}$.

We first note that the single term and the sum in $\mathbf{B}_i$ always contain different particles $i \neq j$. Hence, the product of these terms vanishes under the usual molecular chaos assumption $\langle v_{i,x}v_{j,y}\rangle = 0$. If we further use that particles are interchangeable so that $\langle \chi(\Delta u)v_{i,x}v_{i,y}\rangle = \langle \chi(\Delta u)v_{j,x}v_{j,y}\rangle$, we obtain

$$\langle \chi(\Delta u)B_{i,x}B_{i,y}\rangle = \left(\frac{2}{n_\xi}+1\right)\langle \chi(\Delta u)n_x n_y(\hat{\mathbf{n}}\cdot\mathbf{v}_i)^2\rangle.$$

Finally, averaging over $\hat{\mathbf{n}}$ and neglecting higher correlations for particle i, we arrive at

$$\langle \chi(\Delta u)B_{i,x}B_{i,y}\rangle \approx \frac{2}{9}\left(\frac{2}{n_\xi}+1\right)\langle \chi(\Delta u)\rangle\langle v_{i,x}v_{i,y}\rangle. \tag{D1}$$

In the next term $\langle \chi(\Delta u)v_{i,x}A_y\rangle$, we note that the quantity $\mathbf{A}$ also depends on the positions of the particles so that these must be included in the average. We may perform this average over the particle positions separately on $\mathbf{A}$ to obtain

$$\langle \mathbf{A}\rangle = -\left\langle \mathbf{I}_\xi^{-1} m_0 \sum_{\mathbf{x}_{j,c}\in\mathscr{V}_\xi}\left[\left(\mathbf{x}_{i,c}\cdot\mathbf{x}_{j,c}\right)\mathbf{B}_j - \left(\mathbf{B}_j\cdot\mathbf{x}_{i,c}\right)\mathbf{x}_{j,c}\right]\right\rangle$$

$$= -\left\langle \mathbf{I}_\xi^{-1} m_0\left[\mathbf{x}_{i,c}^2 \mathbf{B}_i - \left(\mathbf{x}_{i,c}\cdot\mathbf{B}_i\right)\mathbf{x}_{i,c}\right]\right\rangle$$

$$= -2\langle \mathbf{I}_\xi^{-1}\rangle m_0 \langle x_{i,c}^2\rangle\mathbf{B}_i = -\frac{\mathbf{B}_i}{n_\xi}, \tag{D2}$$

where $x_{i,c}$ denotes any of the components of $\mathbf{x}_{i,c}$. In the last line, we assumed that the contribution of the single particle i is low so that we can average $\langle \mathbf{I}_\xi\rangle = (n_\xi - 1)m_0 a_0^2 \mathbf{I}/6$ separately. Furthermore, we used that $\langle x_{i,c}^2\rangle = a_0^2/12(1 - 1/n_\xi)$ for any of the components of the position $\mathbf{x}_{i,c}$ are uncorrelated.

Putting Eq. (D2) into $\langle \chi(\Delta u)v_{i,x}A_y\rangle$ and using Eq. (39), we obtain

$$\langle \chi(\Delta u)v_{i,x}A_y\rangle = -\frac{\langle \chi(\Delta u)v_{i,x}B_{i,y}\rangle}{n_\xi} \approx \frac{\langle \chi(\Delta u)\rangle\langle v_{i,x}v_{i,y}\rangle}{3 n_\xi}. \tag{D3}$$

We proceed with the term $\langle \chi(\Delta u)B_{i,x}A_y\rangle$. Since the term $B_{i,x}$ does not depend on the position of the particle, we can immediately apply Eq. (D2) and insert Eq. (D1) to arrive at

$$\langle \chi(\Delta u)B_{i,x}A_y\rangle \approx -\frac{2}{9 n_\xi}\left(\frac{2}{n_\xi}+1\right)\langle \chi(\Delta u)\rangle\langle v_{i,x}v_{i,y}\rangle. \tag{D4}$$

The last term to calculate is

$$\langle \chi(\Delta u)A_x A_y\rangle$$

$$= \left\langle \chi(\Delta u)\left[\mathbf{I}_\xi^{-1} m_0 \sum_{\mathbf{x}_{j,c}\in\mathscr{V}_\xi}\left(\mathbf{x}_{i,c}\cdot\mathbf{x}_{j,c}\right)\mathbf{B}_j - \left(\mathbf{B}_j\cdot\mathbf{x}_{i,c}\right)\mathbf{x}_{j,c}\right]_x\right.$$

$$\left.\times \left[\mathbf{I}_\xi^{-1} m_0 \sum_{\mathbf{x}_{k,c}\in\mathscr{V}_\xi}\left(\mathbf{x}_{i,c}\cdot\mathbf{x}_{k,c}\right)\mathbf{B}_k - \left(\mathbf{B}_k\cdot\mathbf{x}_{i,c}\right)\mathbf{x}_{k,c}\right]_y\right\rangle. \tag{D5}$$

Similarly, we separately average $\langle \mathbf{I}_\xi^2 \rangle = (19/360 + (n_\xi - 1)/36)(n_\xi - 1)m_0 a_0^2 \mathbf{I} \approx (n_\xi - 1)^2 m_0 a_0^2 \mathbf{I}/36$ based on the assumption of molecular chaos and that the contribution of single pairs of particles is small. Multiplying out yields three terms,

$$
\langle \chi(\Delta u) A_x A_y \rangle
$$
$$
= \langle \mathbf{I}_\xi^{-2} \rangle m_0^2 \Bigg\langle \chi(\Delta u) \sum_{\mathbf{x}_{j,c}, \mathbf{x}_{k,c} \in \mathscr{V}_\xi} \Bigg[B_{j,x} B_{k,y} \sum_\alpha x_{i,c,\alpha}^2 x_{j,c,\alpha} x_{k,c,\alpha}
$$
$$
- 2 \sum_{\alpha,\beta} x_{i,c,\alpha} x_{j,c,\alpha} B_{j,x} B_{k,\beta} x_{i,c,\beta} x_{k,c,y} \Bigg] \Bigg\rangle, \tag{D6}
$$

of which the last is zero because $\langle x_{j,x} x_{k,y} \rangle = 0$ for all j, k. We continue with the averages over the positions inside the sums. In the first summand of Eq. (D6), we recognize that $\langle x_{j,c,\alpha} x_{k,c,\alpha} \rangle = \langle x_{j,c,\alpha}^2 \rangle \delta_{kj}$, and in the second one, we may rewrite $\langle x_{i,c,\alpha} x_{i,c,\beta} \rangle = \langle x_{i,c,\alpha}^2 \rangle \delta_{\alpha\beta}$ and $\langle x_{j,c,\alpha} x_{k,c,y} \rangle = \langle x_{j,c,\alpha}^2 \rangle \delta_{\alpha y} \delta_{kj}$. This follows from the usual molecular chaos assumption that different particles are uncorrelated and the assumption that the components of a position are also uncorrelated. Performing the sums with these replacements, we obtain

$$
\langle \chi(\Delta u) A_x A_y \rangle
$$
$$
= \langle \mathbf{I}_\xi^{-2} \rangle m_0^2 \Big\langle \chi(\Delta u) 3 B_{j,x} B_{j,y} \big[(n_\xi - 1)\langle x_{i,c}^2 \rangle^2 + \langle x_{i,c}^4 \rangle \big]
$$
$$
- 2 B_{i,x} B_{i,y} \big[(n_\xi - 1)\langle x_{i,c}^2 \rangle^2 + \langle x_{i,c}^4 \rangle \big] \Big\rangle
$$
$$
= \langle \mathbf{I}_\xi^{-2} \rangle m_0^2 \big[(n_\xi - 1)\langle x_{i,c}^2 \rangle^2 + \langle x_{i,c}^4 \rangle \big] \langle \chi(\Delta u) B_{i,x} B_{i,y} \rangle. \tag{D7}
$$

For the term $\langle \chi(\Delta u) B_{j,x} B_{j,y} \rangle$, we may refer to Eq. (D1). If we approximate $\langle x_{i,c}^4 \rangle \approx a_0^4/80$ and $\frac{n_\xi - 1}{4 n_\xi^2} \approx \frac{1}{4 n_\xi}$, we arrive at

$$
\langle \chi(\Delta u) A_x A_y \rangle
$$
$$
= \langle \mathbf{I}_\xi^{-2} \rangle a_0^4 m_0^2 \Bigg[\frac{(n_\xi - 1)^3}{144 n_\xi^2} + \frac{1}{80} \Bigg] \langle \chi(\Delta u) B_{i,x} B_{i,y} \rangle
$$
$$
= \Bigg[\frac{1}{4 n_\xi} + \frac{9}{20(n_\xi - 1)^2} \Bigg] \langle \chi(\Delta u) B_{i,x} B_{i,y} \rangle
$$
$$
\approx \frac{1}{18 n_\xi} \Bigg(\frac{2}{n_\xi} + 1 \Bigg) \langle \chi(\Delta u) \rangle \langle v_{i,x} v_{i,y} \rangle. \tag{D8}
$$

In the last line, we have furthermore neglected the term $\frac{9}{20(n_\xi - 1)^2}$, which is small compared to $\frac{1}{4 n_\xi}$.

DATA AVAILABILITY

The data that support the findings of this study are available from the corresponding author upon reasonable request.

REFERENCES

[1] A. Malevanets and R. Kapral, "Mesoscopic model for solvent dynamics," J. Chem. Phys. **110**, 8605–8613 (1999).

[2] R. Kapral, "Multiparticle collision dynamics: Simulation of complex systems on mesoscales," Adv. Chem. Phys. **140**, 89 (2008).

[3] G. Gompper, T. Ihle, D. Kroll, and R. Winkler, "Multi-particle collision dynamics: A particle-based mesoscale simulation approach to the hydrodynamics of complex fluids," in *Advanced Computer Simulation Approaches for Soft Matter Sciences III* (Springer, 2009), pp. 1–87.

[4] A. Zöttl and H. Stark, "Simulating squirmers with multiparticle collision dynamics," Eur. Phys. J. E **41**, 61 (2018).

[5] G. Rückner and R. Kapral, "Chemically powered nanodimers," Phys. Rev. Lett. **98**, 150603 (2007).

[6] I. O. Götze and G. Gompper, "Mesoscale simulations of hydrodynamic squirmer interactions," Phys. Rev. E **82**, 041921 (2010).

[7] P. de Buyl and R. Kapral, "Phoretic self-propulsion: A mesoscopic description of reaction dynamics that powers motion," Nanoscale **5**, 1337–1344 (2013).

[8] A. Zöttl and H. Stark, Phys. Rev. Lett. **112**, 118101 (2014).

[9] J. Blaschke, M. Maurer, K. Menon, A. Zöttl, and H. Stark, Soft Matter **12**, 9821–9831 (2016).

[10] T. Eisenstecken, J. Hu, and R. G. Winkler, "Bacterial swarmer cells in confinement: A mesoscale hydrodynamic simulation study," Soft Matter **12**, 8316–8326 (2016).

[11] M. Wagner and M. Ripoll, "Hydrodynamic front-like swarming of phoretically active dimeric colloids," Europhys. Lett. **119**, 66007 (2017).

[12] M. Theers, E. Westphal, K. Qi, R. G. Winkler, and G. Gompper, "Clustering of microswimmers: Interplay of shape and hydrodynamics," Soft Matter **14**, 8590–8603 (2018).

[13] A. Zöttl and J. M. Yeomans, "Enhanced bacterial swimming speeds in macromolecular polymer solutions," Nat. Phys. **15**, 554–558 (2019).

[14] F. J. Schwarzendahl and M. G. Mazza, "Maximum in density heterogeneities of active swimmers," Soft Matter **14**, 4666–4678 (2018).

[15] F. J. Schwarzendahl and M. G. Mazza, "Hydrodynamic interactions dominate the structure of active swimmers' pair distribution functions," J. Chem. Phys. **150**, 184902 (2019).

[16] J.-T. Kuhr, F. Rühle, and H. Stark, "Collective dynamics in a monolayer of squirmers confined to a boundary by gravity," Soft Matter **15**, 5685–5694 (2019).

[17] A. W. Zantop and H. Stark, "Squirmer rods as elongated microswimmers: Flow fields and confinement," Soft Matter **16**, 6400–6412 (2020).

[18] F. Rühle and H. Stark, "Emergent collective dynamics of bottom-heavy squirmers under gravity," Eur. Phys. J. E **43**, 26 (2020).

[19] P. Kanehl and H. Stark, "Self-organized velocity pulses of dense colloidal suspensions in microchannel flow," Phys. Rev. Lett. **119**, 018002 (2017).

[20] P. Kanehl and H. Stark, "Hydrodynamic segregation in a bidisperse colloidal suspension in microchannel flow: A theoretical study," J. Chem. Phys. **142**, 214901 (2015).

[21] J. Padding and A. Louis, "Hydrodynamic and Brownian fluctuations in sedimenting suspensions," Phys. Rev. Lett. **93**, 220601 (2004).

[22] A. Moncho-Jordá, A. Louis, and J. Padding, "Effects of interparticle attractions on colloidal sedimentation," Phys. Rev. Lett. **104**, 068301 (2010).

[23] M. Yang, A. Wysocki, and M. Ripoll, "Hydrodynamic simulations of self-phoretic microswimmers," Soft Matter **10**, 6208–6218 (2014).

[24] A. Malevanets and J. M. Yeomans, "Dynamics of short polymer chains in solution," Europhys. Lett. **52**, 231 (2000).

[25] A. Zöttl and J. M. Yeomans, "Driven spheres, ellipsoids and rods in explicitly modeled polymer solutions," J. Phys.: Condens. Matter **31**, 234001 (2019).

[26] K. Qi, E. Westphal, G. Gompper, and R. G. Winkler, "Enhanced rotational motion of spherical squirmer in polymer solutions," Phys. Rev. Lett. **124**, 068001 (2020).

[27] H. Noguchi and G. Gompper, "Shape transitions of fluid vesicles and red blood cells in capillary flows," Proc. Natl. Acad. Sci. U. S. A. **102**, 14159–14164 (2005).

[28] D. Alizadehrad, T. Krüger, M. Engstler, and H. Stark, "Simulating the complex cell design of *Trypanosoma brucei* and its motility," PLoS Comput. Biol. **11**, e1003967 (2015).

[29] C. Hemelrijk, D. Reid, H. Hildenbrandt, and J. Padding, "The increased efficiency of fish swimming in a school," Fish Fish. **16**, 511–521 (2015).

[30] E. Tüzel, G. Pan, T. Ihle, and D. M. Kroll, "Mesoscopic model for the fluctuating hydrodynamics of binary and ternary mixtures," Europhys. Lett. **80**, 40010 (2007).

[31] T. Hiller, M. S. de La Lama, and M. Brinkmann, "Stochastic rotation dynamics simulations of wetting multi-phase flows," J. Comput. Phys. **315**, 554–576 (2016).

[32] T. Eisenstecken, R. Hornung, R. G. Winkler, and G. Gompper, "Hydrodynamics of binary-fluid mixtures—An augmented multiparticle collison dynamics approach," Europhys. Lett. **121**, 24003 (2018).

[33] K.-W. Lee and M. G. Mazza, "Stochastic rotation dynamics for nematic liquid crystals," J. Chem. Phys. **142**, 164110 (2015).

[34] T. N. Shendruk and J. M. Yeomans, "Multi-particle collision dynamics algorithm for nematic fluids," Soft Matter **11**, 5101–5110 (2015).

[35] S. Mandal and M. G. Mazza, "Multiparticle collision dynamics for tensorial nematodynamics," Phys. Rev. E **99**, 063319 (2019).

[36] K. Rohlf, S. Fraser, and R. Kapral, "Reactive multiparticle collision dynamics," Comput. Phys. Commun. **179**, 132–139 (2008).

[37] C.-C. Huang, G. Gompper, and R. G. Winkler, "Hydrodynamic correlations in multiparticle collision dynamics fluids," Phys. Rev. E **86**, 056711 (2012).

[38] A. Lamura, G. Gompper, T. Ihle, and D. M. Kroll, "Multi-particle collision dynamics: Flow around a circular and a square cylinder," Europhys. Lett. **56**, 319 (2001).

[39] E. Westphal, S. P. Singh, C.-C. Huang, G. Gompper, and R. G. Winkler, "Multiparticle collision dynamics: GPU accelerated particle-based mesoscale hydrodynamic simulations," Comput. Phys. Commun. **185**, 495–503 (2014).

[40] M. P. Howard, A. Z. Panagiotopoulos, and A. Nikoubashman, "Efficient mesoscale hydrodynamics: Multiparticle collision dynamics with massively parallel GPU acceleration," Comput. Phys. Commun. **230**, 10–20 (2018).

[41] E. Tüzel, M. Strauss, T. Ihle, and D. M. Kroll, "Transport coefficients for stochastic rotation dynamics in three dimensions," Phys. Rev. E **68**, 036701 (2003).

[42] E. Tüzel, T. Ihle, and D. M. Kroll, "Constructing thermodynamically consistent models with a non-ideal equation of state," Math. Comput. Simul. **72**, 232–236 (2006).

[43] T. Ihle, E. Tüzel, and D. M. Kroll, "Consistent particle-based algorithm with a non-ideal equation of state," Europhys. Lett. **73**, 664 (2006).

[44] I. O. Götze, H. Noguchi, and G. Gompper, "Relevance of angular momentum conservation in mesoscale hydrodynamics simulations," Phys. Rev. E **76**, 046705 (2007).

[45] H. Noguchi and G. Gompper, "Transport coefficients of off-lattice mesoscale-hydrodynamics simulation techniques," Phys. Rev. E **78**, 016706 (2008).

[46] In our analytic calculations in the following sections we always make the approximation that it coincides with the cell center.

[47] S. K. Upadhyay, *Chemical Kinetics and Reaction Dynamics* (Springer Science & Business Media, 2007).

[48] J.-P. Hansen and I. R. McDonald, *Theory of Simple Liquids* (Elsevier, 1990).

[49] T. Ihle and D. Kroll, "Stochastic rotation dynamics: A Galilean-invariant mesoscopic model for fluid flow," Phys. Rev. E **63**, 020201 (2001).

[50] N. Kikuchi, C. M. Pooley, J. F. Ryder, and J. M. Yeomans, "Transport coefficients of a mesoscopic fluid dynamics model," J. Chem. Phys. **119**, 6388–6395 (2003).

[51] This follows from the definition $\mathbf{v}_\xi = \sum_j \mathbf{v}_i / n_\xi$, taking the average over all particles $j \neq i$, and using $\langle \mathbf{v}_j \rangle = 0$. The last relation also holds for our definition of the shear flow being symmetric about the cell center since the particle can be anywhere in the collision cell.

[52] M. P. Allen and D. J. Tildesley, *Computer Simulation of Liquids* (Oxford University Press, Oxford, 2017).

[53] J. A. Backer, C. P. Lowe, H. C. J. Hoefsloot, and P. D. Iedema, "Poiseuille flow to measure the viscosity of particle model fluids," J. Chem. Phys. **122**, 154503 (2005).

[54] A. Zöttl, "Hydrodynamics of mircoswimmer in confinement and in Poiseuille flow," Ph.D. thesis, Technisch Universität Berlin, 2014.

[55] To compare our method to classical MPCD in an example, we consider how the compressibility is reduced by a factor of six at equal Péclet numbers. To achieve this reduction in classical MPCD, the particle number has to be increased by a factor of six from $n_0 = 10$ to 60. However, this also increases the viscosity by a factor of six. Therefore, to keep the Péclet number constant, the active velocities of microswimmers have to be reduced by a factor of six. As a result, the time required for a simulation is increased by a factor of $6 \times 6 = 36$.

This is in contrast to our method, where we increase the particle number from $n_0 = 10$ to 20. To compensate that the collision rate is effectively lowered due to the stochastic collision rule, we further divide the time step by four and typically take $\Delta t / t_0 = 1/200$, which also keeps the viscosity at the same value as the reference case of classical MPCD. Thus, we achieve a decrease in compressibility by a factor of $2 \times 3 = 6$ at an equal Péclet number. In total, the time required for a simulation is increased by a factor of $2 \times 4 = 8$. Additionally, the implementation of our collision rule only resulted in 5% computational overhead compared to classical MPCD, Therefore, our new method reduces the computational effort by a factor of 4.5.